



*Citation for published version:*

Li, G, Jiang, S, Meng, J, Wu, Z, Jiang, H, Fan, Z, Hu, J, Sheng, X, Zhang, D, Schalk, G, Chen, L & Zhu, X 2023, 'Spatio-temporal evolution of human neural activity during visually cued hand movements', *Cerebral cortex (New York, N.Y. : 1991)*, vol. 33, no. 17, pp. 9764-9777. <https://doi.org/10.1093/cercor/bhad242>

*DOI:*

[10.1093/cercor/bhad242](https://doi.org/10.1093/cercor/bhad242)

*Publication date:*

2023

*Document Version*

Peer reviewed version

[Link to publication](#)

This is a pre-copyedited, author-produced version of an article accepted for publication in *Cerebral cortex* following peer review. The version of record Guangye Li, Shize Jiang, Jianjun Meng, Zehan Wu, Haiteng Jiang, Zhen Fan, Jie Hu, Xinjun Sheng, Dingguo Zhang, Gerwin Schalk, Liang Chen, Xiangyang Zhu, Spatio-temporal evolution of human neural activity during visually cued hand movements, *Cerebral Cortex*, Volume 33, Issue 17, 1 September 2023, Pages 9764–9777 is available online at: <https://doi.org/10.1093/cercor/bhad242>

**University of Bath**

## **Alternative formats**

If you require this document in an alternative format, please contact:  
[openaccess@bath.ac.uk](mailto:openaccess@bath.ac.uk)

### **General rights**

Copyright and moral rights for the publications made accessible in the public portal are retained by the authors and/or other copyright owners and it is a condition of accessing publications that users recognise and abide by the legal requirements associated with these rights.

### **Take down policy**

If you believe that this document breaches copyright please contact us providing details, and we will remove access to the work immediately and investigate your claim.



# Spatio-temporal Evolution of Human Neural Activity During Visually-cued Hand Movements

Guangye Li,<sup>1,†</sup> Shize Jiang,<sup>2,†</sup> Jianjun Meng,<sup>1</sup> Zehan Wu,<sup>2</sup> Haiteng Jiang,<sup>3,4</sup> Zhen Fan,<sup>2</sup> Jie Hu,<sup>2</sup> Xinjun Sheng,<sup>1</sup> Dingguo Zhang,<sup>6</sup> Gerwin Schalk,<sup>5,2</sup> Liang Chen<sup>2,\*,§</sup> and Xiangyang Zhu<sup>1,\*,§</sup>

<sup>1</sup>Institute of Robotics, Shanghai Jiao Tong University, Shanghai, China, <sup>2</sup>Department of Neurosurgery of Huashan Hospital, Department of Neurosurgery of Huashan Hospital, Shanghai, China, <sup>3</sup>Department of Neurobiology, Affiliated Mental Health Center & Hangzhou Seventh People's Hospital, Zhejiang University School of Medicine, Hangzhou, China, <sup>4</sup>MOE Frontier Science Center for Brain Science & Brain-Machine Integration, Zhejiang University, Hangzhou, China, <sup>5</sup>Frontier Lab for Applied Neurotechnology, Tianqiao and Chrissy Chen Institute, Shanghai, China and <sup>6</sup>Department of Electronic and Electrical Engineering, University of Bath, Bath, UK

<sup>†</sup>Contribute to this paper equally and should be considered as co-first authors.<sup>§</sup>Co-corresponding authorship.\*Corresponding author:hschenliang@fudan.edu.cn (L. Chen), mexyzhu@sjtu.edu.cn (XY. Zhu).

## Abstract

Making hand movements in response to visual cues is common in daily life. It has been well known that this process activates multiple areas in the brain, but how these neural activations progress across space and time remains largely unknown. Taking advantage of intracranial electroencephalographic (iEEG) recordings using depth and subdural electrodes from 36 human subjects using the same task, we applied single-trial and cross-trial analyses to high-frequency iEEG activity. The results show that the neural activation was widely distributed across the human brain both within and on the surface of the brain, and focused specifically on certain areas in the parietal, frontal, and occipital lobes, where parietal lobes present significant left lateralization on the activation. We also demonstrate temporal differences across these brain regions. Finally, we evaluated the degree to which the timing of activity within these regions was related to sensory or motor function. The findings of this study promote the understanding of task-related neural processing of the human brain, and may provide important insights for translational applications.

**Key words:** intracranial electroencephalography, SEEG/ECOG, neural activation, spatio-temporal evolution, hand movement

## 1 Introduction

2 Imagine stopping the car in response to a red light. Producing  
3 such motor actions in response to visual cues is one of the most  
4 fundamental and essential functions in human daily life (Corbetta  
5 and Shulman, 2002; Botvinick and Cohen, 2014; Ledberg et al.,  
6 2007). Despite being a simple behavior, the spatio-temporal  
7 neural dynamics underlying such visuomotor processing are rather  
8 complex and have remained relatively unexplored (Pesaran et al.,  
9 2018; Bressler and Menon, 2010; Reichenbach et al., 2014).  
10 Therefore, uncovering the corresponding mechanisms of brain  
11 dynamics over spatial and temporal scales during this process is  
12 of critical importance for both human neuroscience and potential  
13 translational applications (Miller et al., 2014; Kopell et al., 2014;

Hauschild et al., 2012; Franklin and Wolpert, 2011; Coon and  
Schalk, 2016; Coon et al., 2016).

Addressing this question is greatly impeded by the lack  
of a neuroimaging technique that can capture neural activity  
with high spatial and temporal resolution across the brain.  
Functional magnetic resonance imaging (fMRI) has excellent  
spatial resolution and can identify functionally active networks  
across the whole brain regions (Zalesky et al., 2014; Bassett et al.,  
2011; Oosterhof et al., 2012; Floyer-Lea and Matthews, 2004).  
However, fMRI is also inherently constrained by its low temporal  
resolution since blood-oxygen-level dependent (BOLD) signals are  
unable to capture fast-changing neural activities across different  
brain sites. Other non-invasive electrophysiologic approaches such  
as electroencephalography (EEG) and magnetoencephalography  
(MEG) provide high temporal resolution covering the entire

surface of the brain and have been used for investigation of large-scale brain networks at the millisecond-level (Brovelli et al., 2015; Sakkalis, 2011; Cohen, 2017; Jerbi et al., 2007; Thurer et al., 2016; de Pasquale et al., 2010). However, these two techniques are still insufficient for characterizing the progression of neuronal activity in rich detail because of the limitations in spatial resolution (typically centimeter scales) (Lebedev and Nicolelis, 2017; Cohen, 1968). Invasive technologies such as single-unit or multi-unit recordings acquired using implanted microelectrode arrays can capture spatially and temporally detailed images of activity near the recording sites. Many studies have used single- or multi-unit recordings to probe the neural dynamics under different visuomotor tasks within a specific brain region (Rao and Donoghue, 2014; Schall, 2015; Perel et al., 2015; Andersen and Cui, 2009; Ledberg et al., 2007; Kuang et al., 2016). However, this technique cannot readily simultaneously investigate the neural dynamics across larger cortical areas or subcortical regions.

Intracranial electroencephalographic (iEEG) recordings using subdural electrodes (electrocorticography, ECoG) or depth electrodes (stereo-electroencephalography, SEEG) in patients with tumor or intractable epilepsy for pre-surgical monitoring sample neural activity at millimeter-spatial and millisecond-temporal resolution across relatively broad brain areas, and hence provide a tool that can be useful for both scientific research and translational applications (Parvizi and Kastner, 2018; Engel et al., 2005; Miller et al., 2010; Schalk et al., 2017a; Bartolomei et al., 2018; Bonini et al., 2014; Li et al., 2022). In addition, iEEG recordings have the ability to capture broadband gamma activity (i.e., activity at >60 Hz), which has been demonstrated to be a reliable indicator of local neuronal activity (Nir et al., 2007; Buzsaki et al., 2012; Manning et al., 2009; Cardin et al., 2009; Ray et al., 2008; Lachaux et al., 2012). With these characteristics, iEEG broadband signals can chart the spatio-temporal evolution of the underlying task-related neurons among the recording sites (Miller et al., 2014; Takahashi et al., 2015; Coon and Schalk, 2016; Pei et al., 2011; Banerjee et al., 2010). While iEEG recordings inevitably have the limitation of sparse sampling, this limitation can be mitigated by recording across different human subjects using the same task. Thus, group analyses with iEEG recordings can provide information about general features of the large-scale spatio-temporal dynamics of the human brain during the common behaviors (Thiery et al., 2020; Betzel et al., 2019; Arnal et al., 2019; Avanzini et al., 2016; Schalk et al., 2017b; Conner et al., 2014; Posner et al., 2014; Keller et al., 2014; Wander et al., 2013; Lachaux et al., 2003).

In this work, we acquired iEEG recordings from a relatively large number of human subjects with the same visually-cued motor task. Using these recordings, we answered critical questions about the spatio-temporal neural dynamics of the human brain during the task using methodologies that embrace the capabilities of the broadband gamma response of iEEG signals, both at the level of single trials as well as across trials. Specifically, in our paper, we first uncover the brain regions involved during a visuomotor process, quantify their degree of involvement in the task, and then determine the large-scale temporal activation sequence of different task-processing brain regions using a single-trial-based method. Finally, we document the possible functions of these brain regions, e.g., neuronal representations as being primarily ‘sensory’ or ‘motor’ within the entire processing chain through the respective activation temporal profile across trials.

## Materials and Methods

### Subjects, Data Recordings, and Tasks

We acquired iEEG data from 36 right-handed subjects (14 female, 22 male, age:  $26.0 \pm 6.2$  years). The subjects were patients with intractable epilepsy who had depth (SEEG) or subdural (ECoG) electrodes implanted for pre-surgical assessment of their seizure focus. 34 patients had SEEG electrodes and 2 patients had ECoG electrodes (see also Supplementary Table 1). All configurations of implantation were determined by clinical needs rather than the needs of research. SEEG and ECoG signals were acquired during the monitoring period in the hospital using a clinical recording system (EEG-1200C, Nihon Kohden, Irvine, CA) with sampling rates of 500-2000 Hz. All subjects participated in a visually-cued finger and arm movements task that was previously described in Li et al. (2018). In brief, in each trial, subjects were instructed by a visual stimulus presented on an LCD screen to rest for 4 s without any movement, before a visual cue appeared for 1 s to inform the subjects of an upcoming movement. After that, a picture of a gesture appeared for 5 s, and subjects were instructed to repetitively perform that gesture as soon as possible until the disappearance of the picture. For each subject, we collected 100 trials in total ( $\sim 16.67$  mins, Supplementary Fig. 1). During the experiment, the subjects used the hand (L=15, R=21) contralateral to the hemisphere with the majority of the implanted electrodes. Electromyographic (EMG) signals were recorded simultaneously (using the same amplifier and the same sampling rate as the iEEG signals) from the extensor carpi radialis muscle of the moving hand using two surface EMG electrodes. All recorded electrophysiological data exhibiting pathological activity were discarded from the present study. This study was approved by the Ethics Committee of Huashan Hospital (Shanghai, China, Approval ID: KY2019518) and was conducted in accordance with the Declaration of Helsinki. All subjects gave informed consent for this study.

### Electrode Localization

The 36 subjects had a total of 4986 electrodes implanted; the 34 SEEG subjects had a total of 4536 depth electrode contacts implanted ( $133 \pm 40$  contacts and  $10 \pm 3$  electrode shaft on average, 11/9 subjects were implanted on the left/right hemisphere, respectively, and 14 subjects were implanted bilaterally, see Supplementary Table 1) and 2 ECoG subjects had a total of 450 subdural electrodes implanted (242/208 in the left hemisphere). Each SEEG electrode shaft was 0.8 mm in diameter and contained 8-16 contacts along the shaft; each contact was 2 mm long with a 3.5 mm center-to-center spacing distance (Huake Hengsheng Medical Corp., Beijing, CN). ECoG electrodes were 1.8 mm in diameter with a 5 mm inter-electrode distance (Huake Hengsheng Medical Corp., Beijing, CN). The location of all electrodes was identified in each individual brain model using pre-implant MRI and post-implant CT images (Li et al., 2019). In addition, we identified the anatomical location for each electrode using Freesurfer’s cortical parcellation and subcortical segmentation under the Desikan-Killiany atlas (Desikan et al., 2006; Fischl et al., 2002). Moreover, SEEG electrodes located at superficial white matter (i.e., the white matter that is closest to the layer of divided cortical regions, e.g., pre/post-central white matter, up to 36 regions) were identified as well using white matter segmentation results from the Freesurfer (Salat et al., 2009; Guevara et al., 2017; Oishi et al., 2008) and were used in this work, based on the findings

that white matter also presented similar neural activation with the gray matter under tasks (Ding et al., 2018; Li et al., 2021, 2022). The electrodes from the same anatomical regions (both cortical and subcortical) were identified and grouped for further analysis. Finally, we mapped the electrodes from each subject to a standard brain model (Montreal Neurological Institute (MNI)) for subsequent group analyses (Collins et al., 1994). All localization procedures were incorporated into the iEEGview toolbox (Li et al., 2019). The location and related anatomical information of electrodes from all 36 subjects were illustrated in Supplementary Fig. 2.

### Data Pre-Processing

For all the obtained recordings in each subject, we first removed the channels whose line noise power at 50 Hz was larger than a subject-specific cut-off threshold from further analysis. Specifically, the line noise power for each channel ( $LN$ ) was computed as the mean value of absolute line noise signals (filtered signals using a 2<sup>nd</sup> order IIR peak filter at 50 Hz, *iirpeak* in MATLAB) across the entire recording session and the cut-off threshold ( $T_{cutoff}$ ) for each subject was defined as the median line noise power across all channels within the subject plus 10 times of their median absolute deviation ( $T_{cutoff} = median(LN_{all}) + 10 \cdot mad(LN_{all})$ ). This procedure eliminated 48 (0.96%) out of the total of 4986 channels from further analyses (see also Supplementary Table 1). In the second step, all signals were subjected to a 50 Hz comb notch filter to remove line noise and its harmonics (*iircomb* in MATLAB with a quality (Q) factor of 25). We then high-pass filtered the signals at 0.5 Hz using a 6<sup>th</sup> order Butterworth filter to remove slow signal drifts and re-referenced the filtered signals using a Laplacian montage to improve the signal quality (Li et al., 2018; Liu et al., 2021). Finally, we extracted broadband gamma power (BGP) from the processed signals (Voytek et al., 2015; Ries et al., 2017). In detail, we band-pass filtered the re-referenced signals between 60-140 Hz using a 6<sup>th</sup> order Butterworth filter. We then applied the Hilbert transform ( $Hb$ ) of the filtered signal  $s(t)$  to get the analytic signal (Eq. 1).

$$s(t) + iHb[s(t)] = a(t)e^{i\varphi(t)} \quad (1)$$

where the  $a(t)$  and  $\varphi(t)$  were the instantaneous amplitude and instantaneous phase of the analytic signals respectively.

The BGP was then computed as the square of the instantaneous amplitude, and the resulting signals were resampled to 200 Hz to improve computational efficiency. The results of this procedure were subjected to all subsequent analyses (termed as  $G(t)$  in this work,  $G(t) = |a(t)|^2$ ).

For the purpose of subsequent analyses, EMG activity was processed separately to determine the onset of the subject's movement during the task. To do this, we first band-pass filtered (55-145 Hz, 6<sup>th</sup> order Butterworth filter) the two EMG channels to extract the fast-changing neural activity and subtracted the results from each other. Then, for each trial, a joint detection algorithm was applied to identify the onset time of EMG activity. Specifically, we detected the first time point where absolute EMG activity exceeded 1.5 times the average absolute value of EMG activity in the motion period (Li et al., 2018). Additionally, we also detected the time point when the absolute value of EMG activity first time exceeded an adaptive threshold using the envelope of the processed EMG activity (Sedghamiz, 2018). The EMG onset time

in each trial was defined as the earlier time point between these two detections. As a result, the median EMG onset time across all trials and all subjects was 565 ms.

For each trial, three time segments of interest that carried the most representative neural information (i.e., baseline period, task period, and detection period) were defined and adopted in further analysis. Specifically, the baseline period in each trial was defined as the 1 s time interval at the end of the rest period before the onset of the cue, the task period was defined as the first 2 s of the 5-s motion period, and the detection period was defined as the time interval from the appearance of movement cue to 400 ms after EMG activity onset. The task period was used here for more robust detection of the channels presenting task-related modulations (described below). The detection period was selected for the neural activation detection (described below) since it could cover the first complete visuomotor process at the same time minimize the interference from the following continuous movements (e.g., the second movement).

### Detection of Task-related Channels

For each subject, we identified the channels that changed their broadband gamma activity significantly during the task compared to baseline using the same method introduced in our previous work (Li et al., 2018). In brief, we first computed the median values of BGP ( $G(t)$ ) for the baseline and task periods in each trial, respectively (100 trials for each period), and correlated those 200 power values with the baseline/task labels (Spearman correlation coefficient), thus producing a correlation value ( $r$ ) representing the observed relationship of power changes with the movement states. We then performed a randomized permutation test with 2500 repeats to generate a Gaussian distribution of 2500 surrogate  $r$  values, where the task/baseline labels within each channel were randomly shuffled in each repeat and the corresponding  $r$  value was computed (Schalk et al., 2007). The computed channel was considered statistically significant when the  $p$  value (Bonferroni corrected) of the observed  $r$  was within the 1st percentile of the Gaussian distribution (Supplementary Fig. 3). This process identified 1149 (23.0%) task-related channels from all 4986 electrodes. Additionally, using the  $p$  value derived in the permutation test, we also computed the correlation value between each channel and the task ( $-\log_{10}(p)$ , Schalk et al. (2007)). These task-related channels were distributed across 31 different regions of interest (ROIs, Fig. 1d). Finally, we obtained two ratios of task-related neural activation for each of these ROIs by dividing the number of task-related channels with either the total number of channels in the same anatomical region or the total number of all task-related channels from all subjects.

### Detection of Neural Activation Time

The neural processing underpinning a visuomotor task is generally very fast and may last for hundreds of milliseconds (Brovelli et al., 2015; Rao and Donoghue, 2014). Therefore, uncovering the spatio-temporal neural dynamics underlying such behavior tasks asks for a high temporal resolution detection algorithm that can accurately capture the neural population activity in a short time duration. Detection using neural activity in each single trial has been proven to have higher temporal precision than using trial-averaged signals (Coon and Schalk, 2016; Perel et al., 2015; Coon et al., 2016) and its importance in probing brain activities has been addressed previously (Rey et al., 2015).

In this work, we captured the neural activation time for each task-related channel using a single-trial detection algorithm that was described in Paraskevopoulou et al. (2021). In brief, the algorithm finds in each single trial the first peak exceeding a channel- and trial-specific amplitude threshold within the detection period. Specifically, the detection consisted of several steps. In the 1<sup>st</sup> step, we z-scored the BGP activities in each trial for each identified task-related channel (described above). In the 2<sup>nd</sup> step, we applied the normalized BGP of each trial with a non-linear energy operator (NEO,  $\psi$ ) to boost the signal-to-noise ratio (SNR) and facilitate the detection (Eq. 2, Koutsos et al. (2013); Maragos et al. (1993)). In the 3<sup>rd</sup> step, using the transformed BGP ( $\psi[G(t)]$ ) of each channel in the baseline and detection period (Methods: Data Pre-processing), we then determined a channel-specific threshold using an optimization procedure (Eq. 3). More specifically, this procedure updated the threshold value from 2 to 8 with 0.1 increments, and then selected the amplitude threshold maximizing the difference between the number of peaks exceeding the assigned threshold in the detection period and the baseline period. However, considering that the amplitude of  $\psi[G(t)]$  during the task in some active trials may not exceed such a channel-specific threshold, we additionally determined for these trials with undefined detections a trial-specific threshold by implementing another optimization procedure in the 4<sup>th</sup> step. The procedure varied the threshold value between 2 and the identified channel-specific threshold with 0.1 increments, and then selected the threshold that maximized the difference (indicated by the smallest  $p$  value, Wilcoxon rank sum test) between the amplitude distribution of time points comparing with the threshold (represented by logical vectors, e.g., 1 if the amplitude larger than the threshold, else 0) in the detection period and the baseline period. In case the maximal amplitude of  $\psi[G(t)]$  during the task in this trial exceeded the channel-specific threshold, the trial-specific threshold was the same as the identified channel-level threshold (3<sup>rd</sup> step). Specially, if the number of  $\psi[G(t)]$  exceeding the threshold from the baseline period was more than that from the detection period in a trial, no neural activation detection was defined in that location for that trial. With this channel- and trial-specific amplitude threshold, this procedure produced at most one neural activation detection in each trial and for each channel (Supplementary Fig. 3).

$$\psi[G(t)] = \left( \frac{dG(t)}{dt} \right)^2 - G(t) \cdot \left( \frac{d^2G(t)}{dt^2} \right) \quad (2)$$

$$\arg \max_{z=2,2.1,\dots,8} f(\psi_z) := dt(\psi_z) - db(\psi_z) \quad (3)$$

where  $\psi_z$  is the threshold,  $dt(\psi_z)$  and  $db(\psi_z)$  are the numbers of detection in the detection and baseline period, respectively.

For each task-related channel, the time of detected neural activation was then normalized within each trial (e.g., divided by the EMG onset in the same trial) to facilitate further group analyses across subjects. After that, we fit the normalized activation time of each channel with a Gaussian model (Fig. 2c, f, i, and l, Eq. 4), producing for each channel a mean activation time value ( $\mu$ ) and a standard deviation of neural activation ( $\sigma$ ) separately (Fig. 2, see also Supplementary Fig. 3 for the illustration of data processing in this section).

$$f(x) = a * e^{-\frac{(x-\mu)^2}{\sigma^2}} \quad (4) \quad 317$$

where  $\mu$  and  $\sigma$  are the mean value and the standard deviation of the random variable  $X$ ,  $a$  indicates the amplitude of the fitting model ( $f(x)$ ). 318 319 320

With these fitting results, we further excluded the noisy task-related channels from the following analysis. Specifically, we removed from the successful fittings whose  $\sigma$  value was larger than a specific threshold, where the threshold was set as 0.80 after manual inspection across all channels. The operation was based on the assumption that when the task was consistent, the neural activation of task-related channels should be also relatively stable (as measured by  $\sigma$ , Eq. 4). This process identified 564 channels with valid detection across all task-related channels; we labeled these channels as informative channels in this work. Finally, the informative channels from the same anatomical region (see Methods: Electrode Localization) were grouped separately. This step identified 27 regions from 31 different task-related ROIs. Using these informative channels, we computed the average activation time for each ROI group. The average activation time for each ROI was calculated as the real estimated time lag after stimulus onset for illustration purposes. To do that, we multiplied the average normalized activation time of each ROI by the average EMG onset (565 ms). During the calculation, only the ROIs whose number of samples exceeded the median sample numbers (e.g.,  $n=10$ ) of all ROIs were used in order to make the analysis more robust. This process identified 16 of all 27 ROIs. We termed these refined ROIs as informative ROIs ( $n=16$ ) and used them for the subsequent analysis. 321 322 323 324 325 326 327 328 329 330 331 332 333 334 335 336 337 338 339 340 341 342 343 344

Moreover, we also implemented another brain segmentation method which divided the brain into 7 main areas (Del Percio et al., 2019), including the occipital, parietal, frontal, temporal and central area, insula cortex, and limbic system (Supplementary Table 2). This operation produced a more macro assessment of the spatio-temporal evolution of the neural activities within the human brain under the task. Using the same criteria (e.g., the number of samples for each area should be larger than 10), we identified 6 of such 7 areas and computed the corresponding mean activation time for each area. 345 346 347 348 349 350 351 352 353 354

## Activation Pattern Evaluation 355

The single-trial detection method makes it possible to evaluate the activation pattern (that is, neural activation temporal profile across trials) for each informative channel. In this section, we first investigated whether there is a certain relationship between the activation time of informative channels and their activation pattern. Then, we evaluated for each informative channel whether the timing of neural activation suggested that this channel was more related to sensory processing or motor response. Different analyses were performed respectively to answer these two questions. 356 357 358 359 360 361 362 363 364 365

For the first question, we determined the correlation of each informative channel with the response or stimulus by separately correlating (using Pearson's correlation) the raw detected neural activation of each informative channel across all trials with either the EMG onsets or stimulus onsets across all trials (the 'response' here indicates the appearance of motor behaviors and is measured with EMG onsets). This process generated two correlation values (i.e., with response or stimulus) for each informative channel. Together with the average normalized activation time of each 366 367 368 369 370 371 372 373 374

informative channel, we separately analyzed the relationship between each two of these three measurements (i.e., one activation time and two correlation values) for all informative channels with a linear regression model.

For the second question, we conducted two additional computations:

1) We checked how the EMG onsets from single trials were correlated with the detected neural activation of different informative channels. The basic notion is that the neural activation of the channels that are related to the motor response should correlate with the EMG onsets. To investigate this, we implemented a random permutation procedure using the detected neural activation for each channel. In brief, we first computed Pearson's correlation  $r$  for the detected neural activation of each channel and the EMG onsets from all trials. We then randomly shuffled the sequence of detected neural activation and computed the correlation with the EMG onsets for each repetition. This procedure was repeated 2500 times, thus, generating a distribution of surrogate  $r$  value and the subsequent  $p$  value for the observed  $r$  (Supplementary Fig. 3). The channel whose  $p$  value was smaller than the significance level ( $p < 0.05$  after Bonferroni correction of channel numbers) was identified as response-locked channels (see Fig. 2h and 2k as examples);

2) For the same channel, we then conducted another analysis to determine whether this channel was related to sensory processing (termed as the stimulus-locked channel in this work). Our assumption was that detected neural activation of the channels relating to the sensory processing should be time-locked to the stimulus onsets and have small variability on the time of neural activation across trials irrespective of the EMG onsets. To identify stimulus-locked channels, for each informative channel, we computed the standard deviation ( $v$ ) of detected neural activation from a certain number of trials (e.g., 60), which were randomly selected from all trials. This setting was implemented to attenuate the influence of some noisy trials. Then, this process was repeated for  $10^6$  times and the average standard deviation ( $\bar{v}$ ) was obtained for each channel (Supplementary Fig. 3). After this, we then determined a threshold value to filter out the channels with large variations of detected neural activation. To do this, we concatenated all the detected neural activation from all valid channels together and conducted the same random selection process as the single channel to obtain an overall distribution for  $v$ . The threshold was then identified as the left boundary of 95% confidence interval from the distribution. The channel whose  $\bar{v}$  was smaller than the threshold was identified as the stimulus-locked channel in this work (see Fig. 2b and 2e as examples).

The identified stimulus-locked and response-locked channels were then grouped based on their anatomical locations (16 ROIs, described above). For each ROI, the ratio of stimulus-locked and response-locked channels was calculated respectively by dividing either the number of identified stimulus-locked or the number of identified response-locked channels by the number of informative channels within that group.

## Results

### The Distribution of Neural Activation During The Task

The recording electrodes from all subjects are distributed widely within the entire brain (Supplementary Fig. 2). Among these electrodes, we found that 1149 (23.0%) channels showed significant

BGP changes during the task, and these channels are distributed across multiple regions ( $n=31$ , Fig. 1d, Supplementary Table 2), covering cortical regions (central, frontal, parietal, occipital, temporal area) and also deeper brain structures (e.g., insula cortex (13.6% insula electrodes get activated) and limbic systems (such as 36% electrodes in parahippocampus gyrus and 6.1% electrodes in hippocampus)). Among these regions, several ones including the precentral cortex (PRC,  $n=213$ , 18.5%), supramarginal gyrus (SMG,  $n=115$ , 10.0%), postcentral cortex (i.e., gyrus and sulcus) (POC,  $n=112$ , 9.7%), superior parietal cortex (SPC,  $n=105$ , 9.1%), superior frontal gyrus (SFG,  $n=83$ , 7.2%) and insula cortex (ISC,  $n=51$ , 4.4%), lateral occipital cortex (LOC,  $n=46$ , 4.0%) occupied over 60% of all task-related channels (Fig. 1d).

Overall, within each main brain region (Fig. 1d), several regions, including the central area (e.g., 57.9% of electrodes in PRC and 52.6% of electrodes in POC and 51.8% of electrodes in paracentral cortex (PAC) were activated), parietal area (e.g., 57.7% of electrodes in SPC and 44.1% of electrodes in SMG were activated), occipital area (e.g., 62.2% of electrodes in LOC, 57.6% ( $n=19$ ) of electrodes in pericalcarine cortex (PCC) and 29.0% ( $n=18$ ) of electrodes in lingual gyrus (LGG) were activated), and frontal area (e.g., 33.9% of electrodes in SFG were activated), correlated substantially with the task. Moreover, this phenomenon was further confirmed by the average correlation value of each region with the task (Fig. 1f), where the average correlation value, listed in order from high to low, resulted for the central area ( $n=354$ ,  $15.78 \pm 0.48$  (mean  $\pm$  s.e.)), occipital area ( $n=87$ ,  $13.72 \pm 0.86$ ), parietal area ( $n=279$ ,  $12.05 \pm 0.40$ ), frontal area ( $n=187$ ,  $11.30 \pm 0.53$ ), insula cortex ( $n=55$ ,  $9.29 \pm 0.71$ ), temporal area ( $n=108$ ,  $9.15 \pm 0.44$ ), and limbic system ( $n=51$ ,  $7.77 \pm 0.60$ ), respectively. In detail, the top five regions that had the highest correlation value were LOC ( $17.20 \pm 1.24$ ), POC ( $16.89 \pm 0.88$ ), PRC ( $15.60 \pm 0.60$ ), SFG ( $14.64 \pm 0.98$ ), SPC ( $13.22 \pm 0.71$ ) in order, where the correlation in LOC, POC and PRC were significantly ( $p < 0.05$ , Wilcoxon rank sum test) higher than SPC and the value in SPC was significantly ( $p < 0.05$ ) higher than that in pars opercularis (parsOPE,  $10.03 \pm 1.03$ ). The correlation distribution of each electrode within the standard brain were shown in Fig. 1a-c.

In addition, we also observed significant left hemispheric lateralization on activation in the parietal area, including both SPC (number of task-related/nontask-related channels:  $L=72/21$ ,  $R=33/56$ ,  $p < 0.001$ ,  $\chi^2$  test, FDR corrected) and inferior parietal cortex (IPC,  $L=29/84$ ,  $R=8/85$ ,  $p < 0.05$ ) during the task.

### The Spatio-temporal Evolution of Neural Activation During The Task

Among all task-related channels, we identified 564 informative channels. The anatomical and spatial distribution of these channels were shown in Fig. 1e and 3b-c, respectively. Four typical samples of informative detections were illustrated in Fig. 2. These channels, located at different anatomical regions, show differences in their time of neural activation relative to the EMG onsets as well (Fig. 2). Moreover, these four channels clearly present distinct activation patterns (i.e., time-locked to the stimulus or response), indicating the underlying different roles during the task. The average temporal activation sequence of the identified informative ROIs ( $n=16$ ) in relation to the task processing was shown in Fig. 3a. During the task, the activation of neurons roughly starts from the occipital area and then spreads to the temporal area, parietal area, and the limbic system, afterward, goes forward to the

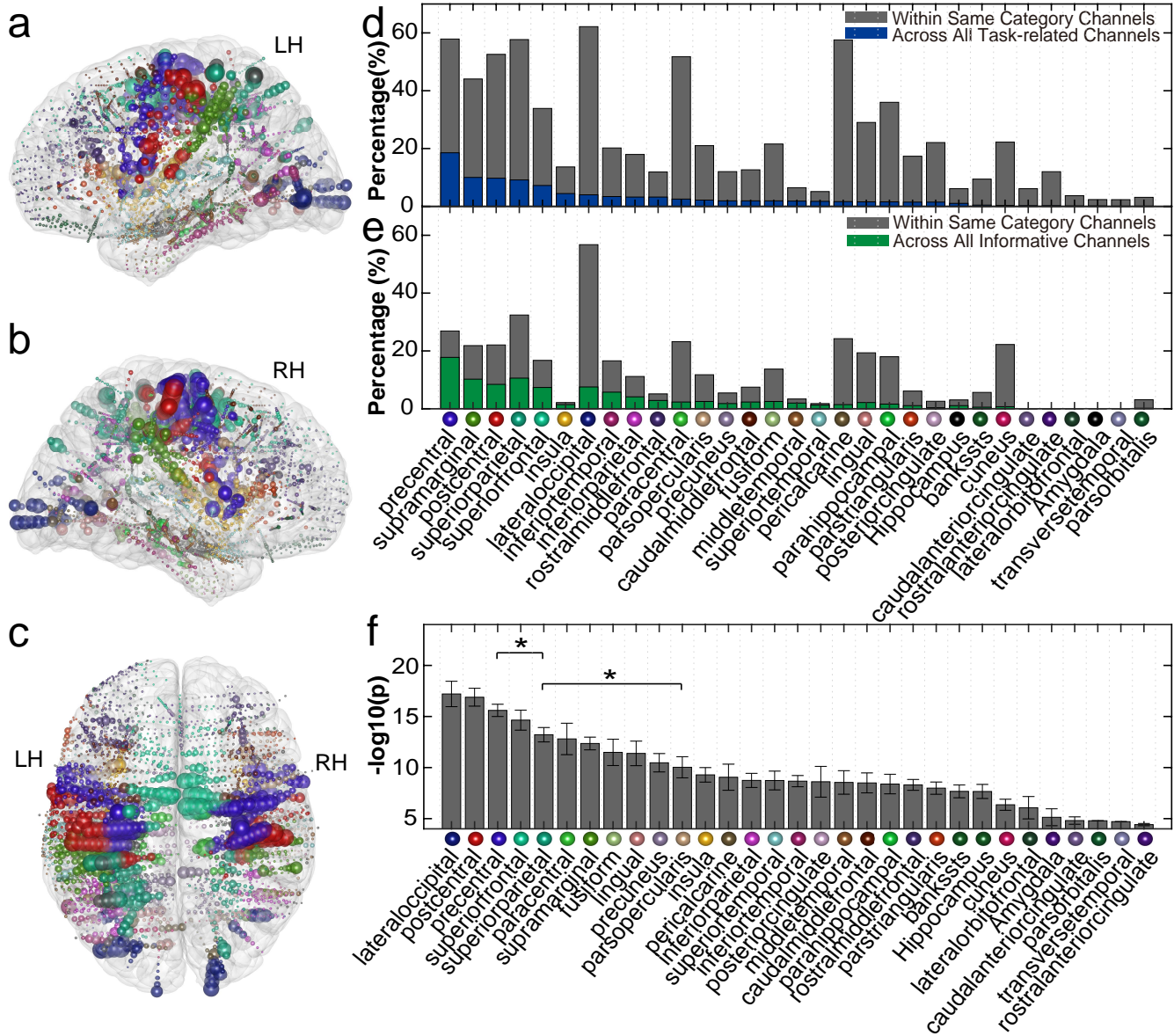


Fig. 1: The distribution of task-related electrodes across all subjects. **a)**/**b)**/**c)** The spatial distribution of task-related electrodes in the MNI brain and their corresponding correlation value with the task (Left/Right/Top view respectively). The electrodes are presented with balls. The color of each ball indicates the anatomical position of that electrode. We used the Desikan-Killiany atlas for brain segmentation. The diameter of the balls corresponds to the correlation value with the task. **d)** The anatomical distribution for all the task-related channels. For each anatomical label (ROI), the gray bar is calculated by dividing the number of task-related channels over the number of channels having the same anatomical label across all subjects, whereas the blue bar is calculated by dividing the number of task-related channels over the number of all task-related channels across all subjects. The anatomical label in the X-axis is encoded using the upper color balls for better visualization. The color of each ball corresponds to the color scheme in (a/b/c). **e)** The anatomical distribution for all the informative channels. The green and gray bars are in the same configuration as the blue and gray bars in (d) but use informative electrodes instead. **f)** The average correlation value ( $-\log_{10}(p)$ ) of each ROI across all subjects. The error bar indicates the standard error. Asterisks denote the significance of the difference between the correlation value of the two ROIs (\*,  $p < 0.05$ , Wilcoxon rank sum test). The anatomical label in the X-axis is encoded using the upper color balls for better visualization. The color of each ball corresponds to the color scheme in (a/b/c).

492 frontal area, and with the central area positioned at the final stages  
 493 (Fig. 3a, see also Supplementary Fig. 4 for the temporal activation  
 494 sequence of different ROIs from four typical single subjects).  
 495 Specifically, LOC ( $n=42$ ,  $183 \pm 6$  ms (mean  $\pm$  s.e.)) activates at the

earliest stage on average after the stimulus onset, indicating the  
 start of visual stimulus processing. Then IPC activates ( $n=23$ ,  
 $229 \pm 17$  ms), and such activation is significantly ( $p < 0.05$ ,  
 Wilcoxon rank sum test) later than the LOC. Following that is

496  
 497  
 498  
 499

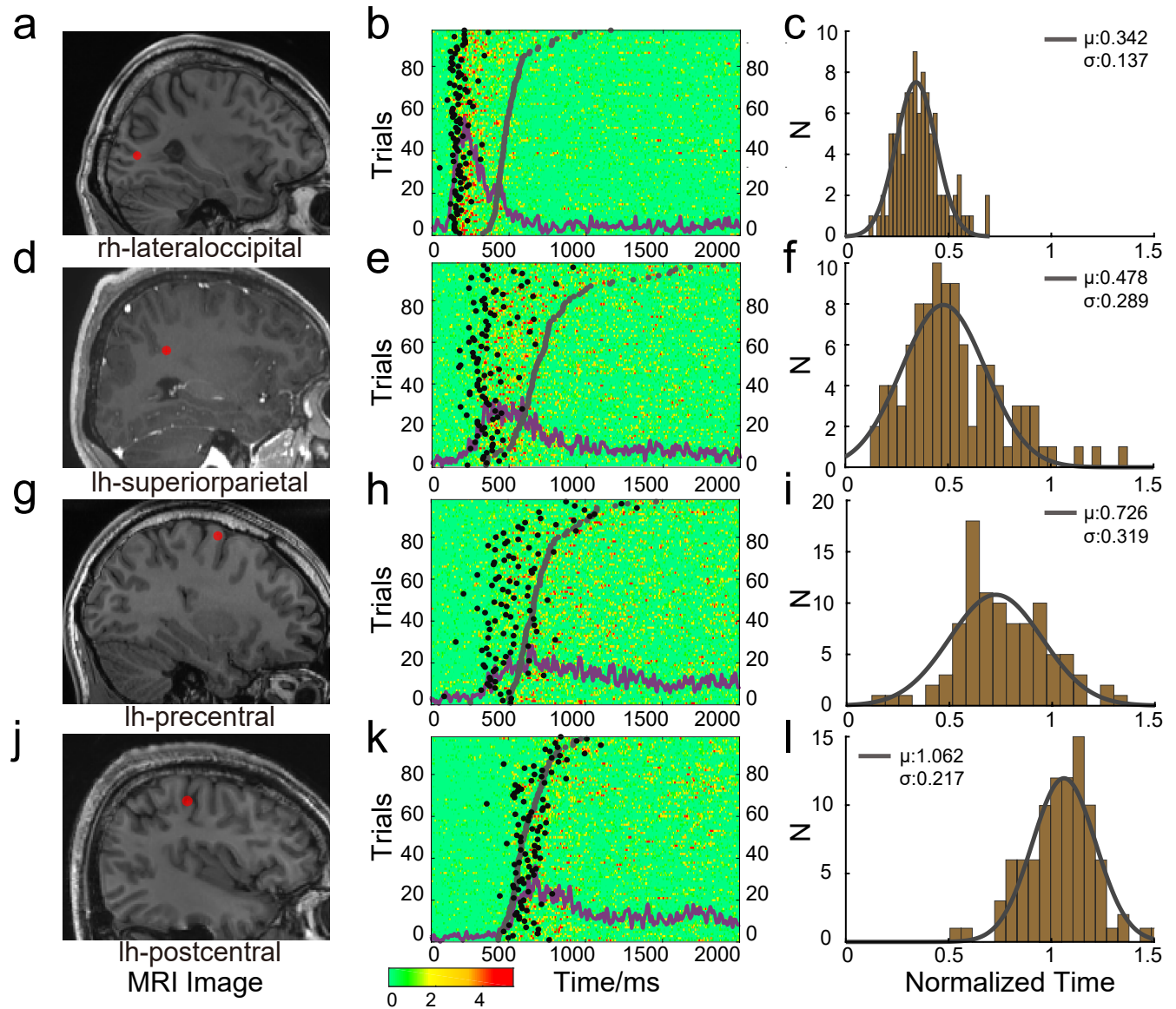


Fig. 2: Illustration of detected neural activation from four typical channels of different subjects. **a)** The position of the electrode on the original MRI image of each single subject. Red dots indicate electrodes. The text below indicates the anatomical position of each electrode. **b)** Single-trial neural activation detection results for the electrode shown in (a). The color map represents the normalized broadband gamma power (BGP) of all trials, where red color indicates higher BGP within each trial. Time zero indicates the onset of the stimulus. The black dot indicates the detected neural activation for each trial. The dark gray dot (Sigmoid shape) indicates the detected EMG onset of each trial. The purple line represents the average normalized BGP across all trials from that channel (the value is magnified by 20 fold for visualization purposes and is shown on the right side of the Y-axis). The detected neural activation and EMG onsets are presented here without normalization to give a better illustration of the difference in neural activation patterns. **c)** The average normalized activation time for the electrode shown in (a). The brown bars indicate the distribution of detected neural activation (after normalization, i.e., divided by the EMG onset in the same trial) from all trials shown in (b). The gray line indicates the curve-fitting result using a Gaussian model.  $\mu$  and  $\sigma$  indicate the mean value and standard deviation of the model. **d-f)/g-i)/j-l)** The detected neural activation for the second/third/fourth channel (d/g/j). The configurations for all these subfigures are the same as (a/b/c). The X-axis of (c/f/i/l) is scaled the same for comparison purposes. lh/rh: left/right hemisphere.

500 the activation from LGG ( $n=12, 247\pm30$  ms), SPC ( $n=59, 251\pm17$  ms), inferior temporal gyrus (ITG,  $n=32, 252\pm10$  ms), fusiform  
 501 ms), inferior temporal gyrus (ITG,  $n=32, 252\pm10$  ms), fusiform  
 502 gyrus (FFG,  $n=14, 254\pm24$  ms), precuneus cortex (PNC,  $n=10,$   
 503  $291\pm32$  ms), middle temporal gyrus (MTG,  $n=11, 291\pm15$  ms),

and rostral middle frontal gyrus (rMFG,  $n=16, 296\pm22$  ms), where  
 504 the SPC activates significantly ( $p < 0.05$ ) earlier than the MTG.  
 505 Then the neural activity goes from SMG ( $n=57, 308\pm15$  ms) to  
 506 the frontal area, including caudal middle frontal gyrus (cMFG,  
 507



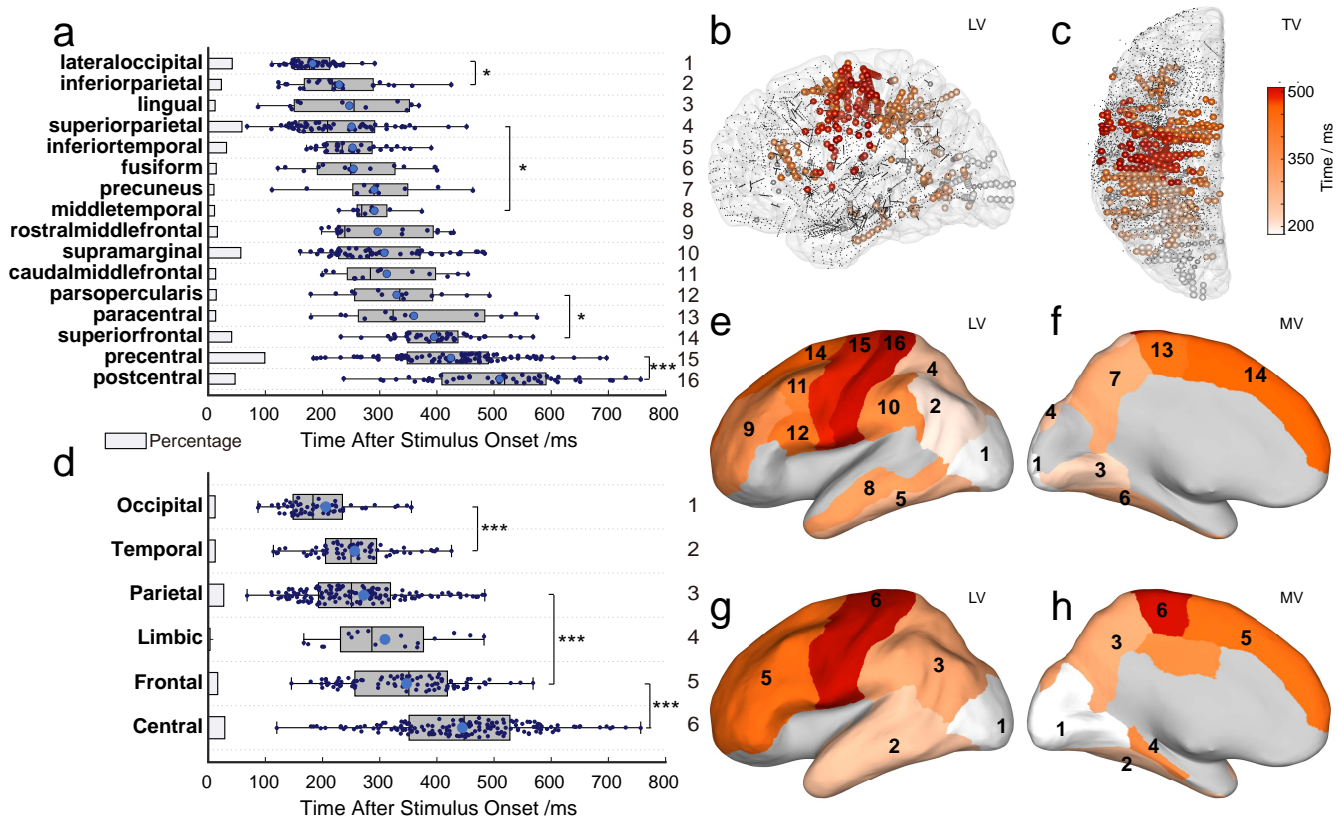


Fig. 3: The spatio-temporal activation results during the task. **a**) The activation time for all the applicable regions of interest (ROIs) during the task processing. For each ROI, the detected neural activation from all informative channels within the ROI was shown (blue dots). Time zero indicates the onset of the stimulus. The activation time shown here is calculated by multiplying the normalized activation time with the average EMG onset time (565 ms). The box indicates the 25 and 75 percentile of all the detected neural activation. The blue dot indicates the mean value. The whiskers extend to the limits of all the detected neural activation within that ROI. The light gray bar on the left indicates the percentage of informative channels belonging to each ROI within all informative channels. The digits on the right side indicate the temporal activation sequence. Statistical analysis are conducted between ROIs (\*,  $p < 0.05$ ; \*\*,  $p < 0.01$ ; \*\*\*,  $p < 0.001$ , Wilcoxon rank sum test). **b**)/**c**) Left/Top view of all the informative electrodes across all subjects in the MNI brain. All the electrodes are projected to the left hemisphere for visualization purposes. The color of electrodes within each ROI is colored using the average activation time of this ROI from (a). **d**) The average activation time for all the applicable 6 areas during the task processing. The other configurations of this subfigure are the same as (a). **e**)/**f**) Left/Middle view of spatio-temporal activation sequence for the 15 ROIs rendering on the flattened MNI brain. Results are shown with the cortical surface of the left hemisphere only. The digits correspond to the results shown in (a). **g**)/**h**) Left/Middle view of spatio-temporal activation sequence for the 6 brain areas rendering on the flattened MNI brain. Activation time is shown on the left hemisphere for illustration purposes. The digits correspond to the results shown in (d). Electrodes located in the hippocampus are used for the computation of the activation time of the limbic system. The hippocampus is not shown in this subfigure.

508  $n=13$ ,  $312 \pm 25$  ms) and parsOP ( $n=14$ ,  $330 \pm 23$  ms) and SFG  
 509 ( $n=41$ ,  $396 \pm 12$  ms), where the parsOPE activates significantly  
 510 ( $p < 0.001$ ) earlier than the SFG. Activation is also detected in  
 511 PAC ( $n=13$ ,  $360 \pm 35$  ms) during this time segment. At the final  
 512 step, the central area activates, where the PRC ( $n=99$ ) activates  
 513 on average at  $424 \pm 11$  ms and significantly ( $p < 0.001$ ) earlier than  
 514 POC ( $n=47$ ,  $510 \pm 18$  ms). The spatio-temporal evolution of neural  
 515 activity during the task was presented in Fig. 3 with the format  
 516 of informative electrodes (3b-c) and cortical regions (3e-f).

517 To give a more macro view on the footprints of neural  
 518 processing during the task, we also computed the mean activation  
 519 time for six different task-related cortical regions in a broader  
 520 area (see Methods: Detection of Neural Activation Time). The

temporal activation sequence for these broader areas was shown  
 in Fig. 3d (see also Supplementary Fig. 5 for the results from  
 four typical single subjects). As can be seen from the figure, the  
 occipital area ( $n=66$ ) gets activated first with a  $206 \pm 10$  ms latency  
 on average after stimulus onset. Following this is the temporal area  
 ( $n=67$ ), which activates at  $256 \pm 9$  ms after stimulus onset. The  
 occipital area activates significantly ( $p < 0.001$ , Wilcoxon rank  
 sum test) earlier than the temporal area. The mean activation time  
 after stimulus onset is  $272 \pm 10$  ms for the parietal area ( $n=149$ ),  
 $309 \pm 24$  ms for the limbic system ( $n=17$ , parahippocampal gyrus  
 $n=9$ ), hippocampus ( $n=6$ ), posterior cingulate gyrus ( $n=2$ )).  
 Then the activation spreads to the front area at a latency of  
 $347 \pm 10$  ms ( $n=91$ ), where the frontal area activates significantly

521  
522  
523  
524  
525  
526  
527  
528  
529  
530  
531  
532  
533

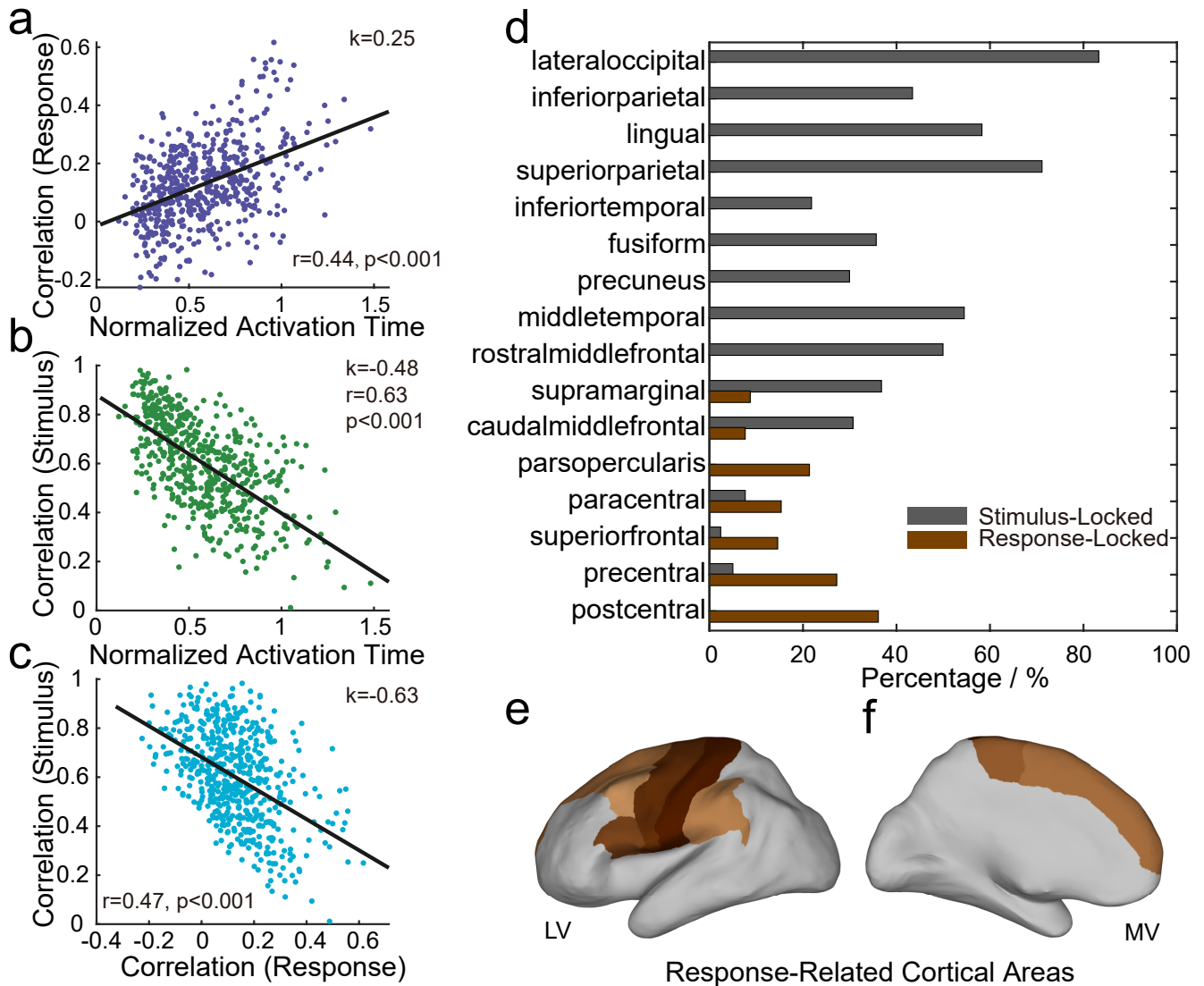


Fig. 4: The activation pattern evaluation results. **a)** The relationship between the activation time and its correlation with the response onsets for each informative channel (see Methods: Activation Pattern Evaluation). Average normalized activation time is used here for each informative channel, where time zero indicates the onset of the stimulus and time one indicates the onset of response (i.e., motor behavior). Each colored dot indicates the result from one informative channel. The black line represents the fitted line generated using the least square method.  $k$  indicates the slope of the fitted line.  $r$  and  $p$  indicate Pearson's correlation values  $r$  and corresponding  $p$  values, calculated between the fitted value and the real value. **b)** The relationship between the activation time and its correlation with the stimulus onsets for each informative channel. The configurations for this subfigure are the same as (a). **c)** The relationship between the correlation with response time and the correlation with stimulus time for each informative channel. The configurations for this subfigure are the same as (a). **d)** Percentage of stimulus-locked and response-locked channels within each ROI. The ROIs are the same as Fig. 3. **e)/f)** Left/Middle view of the distribution of response-locked channels on a flattened MNI brain. Results are shown with the left hemisphere only. The darkness of the colored cortex indicates the percentage value shown in (d). Darker color indicates a higher percentage.

534 ( $p < 0.001$ ) later than the parietal area. At the final stage, the  
 535 central area ( $n=159$ ) gets activated with an average latency at  
 536  $444 \pm 10$  ms, and such activation is significantly ( $p < 0.001$ ) later  
 537 than the frontal area. The temporal evolution of the cortical neural  
 538 activities for these regions is shown in Fig. 3g and 3h.

### The Pattern of Neural Activation During The Task

539  
 540 To investigate the possible role of each informative electrode  
 541 with respect to task processing, we evaluated if there existed a  
 542 certain relationship between the activation time of these channels  
 543 and their correlation with stimulus and/or response onsets. Our  
 544 results show that the channels that activate earlier correlate more  
 545 with the stimulus onsets ( $k = -0.48, r = 0.63, p < 0.001, k$ :

the slope of the fitted line, Fig. 4b), while the channels that activate later tend to correlate more with the response onsets ( $k = 0.25$ ,  $r = 0.44$ ,  $p < 0.001$ , Fig. 4a). Such correlation with the stimulus onsets and the value with the response onsets is reversely correlated ( $k = -0.63$ ,  $r = 0.47$ ,  $p < 0.001$ , Fig. 4c). This result indicates the existence of an at-least two-stage neural process during the task processing, where the first stage is characterized by a stimulus-locked activation pattern, indicating the sensory information processing; the other stage is characterized by a response-locked activation pattern, representing the generation of the motor response.

We then evaluated the percentage of stimulus-locked and response-locked channels detected within each of the informative ROIs. The results show that wide areas of the entire brain, including most parts of the occipital area, the entire parietal area, parts of the temporal, frontal area, and even the central area, present stimulus-locked activation patterns (Fig. 4d). The current observation suggests the importance and complexity of sensory information processing prior to motor execution. More specifically, within these regions, the highest percentage of stimulus-locked channels was found in LOC, reaching 83.3%. Following that, the SPC (71.2%) was also a rich source of producing stimulus-locked activation. As the final stage of the task processing, the central area contained the lowest percentage of stimulus-locked channels (see also Supplementary Fig. 6 for the distribution of these areas). As a comparison, the central area, including POC (36.2%) and PRC (27.3%), has the highest percentage of response-locked channels. Besides, some parts of the frontal area (parsOPE (21.4%), SFG (14.6%), cMFG (7.7%)), a small portion of the parietal area (e.g., SMG (9%)) have also been found contain response-locked channels (Fig. 4d-f), indicating the possible function of these ROIs in relation to the generation of movement.

## Discussion

In this work, using iEEG recordings from 4986 channels and 36 human subjects, we investigated the spatio-temporal dynamics of human cortical activity during a visually-cued motor process. Specifically, we answered three relevant scientific questions by conducting group analyses with high-frequency neural activities. In detail, we first identified the distribution and strength of brain regions involved in task processing. We then extracted the temporal activation sequence of different ROIs during the task. Finally, we analyzed the possible role (e.g., relating to sensory information process or motor response) of each informative ROI involved in the processing chain.

### The Distribution of Neural Activation Within The Brain

We found rather broad regions of neural activation during the current task. Within the task-related regions, the most active regions were observed in the central, parietal, and occipital area, the regions in the frontal area that are close to the PRC, and the inferior part of the temporal area, demonstrating the essential roles of these cortical areas in visuomotor processing. Importantly, besides the lateral direction, we also give an overview of the neural activation along the depth direction (Fig. 1). For instance, the deep brain structures, such as the insula cortex, parahippocampal gyrus, and hippocampus, have also been observed present task-related activation. The current observations further enrich the

findings from previous ECoG (Keller et al., 2014) and MEG studies (Brovelli et al., 2017). Moreover, our results also suggest that the processing of a visuomotor task needs to recruit neural networks spanning brain regions from both cortical and subcortical levels. On this basis, revealing how neural activities interact between cortical and subcortical regions will be interesting and deserves further exploration in the following studies.

Apart from this, this work also gives additional spatial information on the activation of the parietal area, since we have found the existence of significant left lateralization on the activation within this area during the current visuomotor process. The present finding provides valuable implications for future parietal area-based studies, especially the research adopting neural activities from the parietal area for the brain-machine interface purpose (Aflalo et al., 2015; Li et al., 2022; Wang et al., 2020). More importantly, similar phenomena have been also detected under other cognitive processes, including the tool-action observation (Caruana et al., 2017), auditory and visual stimulus processing (Molholm et al., 2006), and visual and motor imagery aspects of hand shape encoding (Klaes et al., 2015). Moreover, such left-lateralized activation is reported to be independent of handedness (Haaland et al., 2004; Vingerhoets et al., 2012; Króliczak and Frey, 2009). Hence, all these observations may together suggest the existence of the action observation/execution network involving this area, which possibly mediates the identification of the basic goal of the observed action for both humans and monkeys (Rizzolatti et al., 2014).

### The Spatio-temporal Evolution of Neural Activation During The Task

In this work, we analyzed and presented the evolution of neural activation across the human brain during a visuomotor task using the neural recordings from all subjects (Fig. 3). The results were further supported by the consistent results observed among the partially-covered ROIs from the individual subjects (see Supplementary Figs. 4 and 5). Roughly, early activation is shown in the lateral part of the occipital area, the superior and posterior part of the parietal area, and the posterior and inferior part of the temporal area. Then, the activation spreads to the frontal area and finally ends with the central area. It is also of interest to compare our data with the results reported by Johnson et al. (1996) and Nishitani and Hari (2000). The former authors studied the activation pathway during a visually guided reach movement with nonhuman primates' single-neuron recordings. They found the activation begins in the visual cortex and passes through the posterior parietal cortex to the dorsal premotor cortex and then to the primary motor cortex. The subsequent study reported the temporal sequence of three ROIs during hand action imitation using MEG recordings, where the visual cortex in the occipital lobe first activates, and then the inferior frontal cortex activates (parsOPE in this work), following that is the activation in the primary motor area (PRC in this work). These results are in good agreement with our ones. Meanwhile, distinct from these studies, our work extends the results to more and wider regions of the entire human brain, and hence can provide a comparatively more intact overview of the 'footprints' of neural activity during the task. It is worth noting that the spatio-temporal sequence reported here should be interpreted carefully since the results are derived from group analysis. Thus, our results cannot detect variations in activation time among subregions of different ROIs or the same

ROIs (Supplementary Fig. 4). At the same time, our results make it clear that there is a definitely consistent temporal sequence across these ROIs.

Notably, although temporal activation sequence results show that POC activates lastly among all the informative ROIs (Fig. 3), the identified POC activation represents more than the somatosensory feedback after motor execution. Because the average activation time of POC ( $510 \pm 18$  ms) in our work is slightly ahead of the movement onset (565 ms on average), indicating that some neurons in POC start firing prior to the movement onset (see also Supplementary Fig. 4a). Such early activation provides further evidence supporting the additional role of the somatosensory cortex in sensory information encoding that relates to the anticipation of movements (Wolpert et al., 1995; Sun et al., 2015).

Besides, we have detected 13.6% ( $n=51$ ) of electrodes located in the insula cortex presenting task-related activation, denoting the substantial involvement of this area during the visuomotor task. However, only a few of them are informative enough ( $n=8$ ,  $395 \pm 44$  ms) for the calculation of activation time. This may be because of the observation that most of the task-related channels in this area tend to activate in an irregular way (i.e., the onsets of activation are distributed sparsely across trials). The neural mechanism behind such neural activation patterns is not well understood yet. Consistently, Bartoli et al. (2018) also reported that the insula cortex exhibits an increase in broadband gamma activity under a button press task but such activation is less robust and later than the inferior frontal cortex (see also Fig. 3). Together, the current results imply that the insula cortex may play an indispensable role in sensory-motor processing, and the detailed function of this area still needs further investigation.

#### The Possible Role of The ROIs During The Task

Within the detected processing chain of the visuomotor task, on the average level, our data support the general understanding that the neurons that activate early tend to correlate more with the visual stimulus delivery, while the neurons holding late activation tend to associate more with the motor response (Fig. 4a-c). Furthermore, we also analyze the neuronal representations as being ‘sensory’ or ‘motor’ for each informative channel based on whether the neural activation is more closely linked to the onset of a stimulus or the initiation of a response (Fig. 4d). The earliest activation and highest percentage of stimulus-locked channels presented in our results demonstrate together the role of the lateral occipital cortex in the visual information processing during the task (Tallon-Baudry et al., 2004; Larsson and Heeger, 2006). Then, a high percentage of stimulus-locked channels in the parietal area and temporal area indicate as well the important function of these areas in visual information processing. Such visual representation gets weak when the process evolves to the frontal and central areas. Moreover, we have also detected obvious involvement from the parietal and frontal areas in the early stage of neural processing relating to the initiation of motor response. Previous reports have consistently suggested that motor function from the parietal area is related to the sensorimotor transformation (Andersen and Cui, 2009), including hand trajectory information (Hauschild et al., 2012) and motor intentions, where the intention in the parietal area may be processed in relation to sensory predictions (Klaes et al., 2015). Whereas the motor function in the frontal area represents higher-level aspects of movement planning and decision

making in relation to motor execution (Rizzolatti et al., 2014; Miller and Cohen, 2001; Schall, 2015). On these bases, our results further enhance the understanding of the critical sensorimotor-related functions for these two areas (Andersen and Buneo, 2002; Corbetta and Shulman, 2002). At the last stage of the neural processing chain, the central area presents the highest percentage of response-locked neural activity, indicating their function in motor execution and somatosensory processing (Scott, 2004; Lemon, 2008). Interestingly, within the central area, we also detect a minority of channels in the PRC that present early stimulus-locked activation (Figs. 4d and 3a). These findings promote the understanding of the intact functions of this motor area, where the view that the PRC is an integral part of a cue-to-action network so as to make immediate responses to environmental stimulus (Rao and Donoghue, 2014), may account for the observation.

Taken together, the neural processing results during the visuomotor task revealed in this work likely support the opinion that visual information is firstly processed and segregated along two pathways (Figs. 1, 3 and 4), where the ventral stream (occipito-temporal cortex) computes vision for perception and the dorsal stream (occipito-parietal cortex) computes vision for action (Culham and Valyear, 2006). The parietal and frontal areas play an important role in the transformation of sensory information to motor-related information. Specifically, the parietal area participates in the early stage of such processing while the frontal area tends to engage more in the motor execution. At the final stage of motor execution, PRC generates motor signals from an already highly processed sensory input and other internal signals, following that is the production of the somatosensory feedback from POC after motor execution (but also see discussion above). Apart from this, we also conducted additional analyses to further investigate whether the reaction time of a subject is associated with the motor cortex only. To do this, we first computed the average reaction time (computed as the trial-averaged EMG onsets within each subject) and the average raw activation time (without normalization) for all informative channels within each informative ROI across subjects. Then, for each informative ROI, we computed a Spearman correlation value between the average reaction time and the average raw activation time for all informative channels within this region. Finally, the ROIs producing significant correlations ( $p < 0.05$ ) were identified. In this analysis, we find that, besides the central area, the activation time from multiple regions, including temporal, parietal, and frontal areas, also correlates significantly with the reaction time of subjects for the current task (results not shown here). This finding denotes that the reaction speed of a human is not attributed to a single region (e.g., the well-known PRC), but an entire task-related brain network including both sensory and motor information processing.

#### Implications, Limitations, and Future Work

The current work presents the overall large-scale spatio-temporal neural evolution of the human brain during a visuomotor task and evaluates the possible functions across different ROIs. The findings from this study enhance the understanding of the neural responses under the task for neuroscientific studies. Moreover, the findings also bring valuable insights for future movement-related brain-machine interface research, which is also a focus of this work (e.g., besides the traditional sensorimotor area, paying additional attention to brain areas such as the frontal and parietal

area for the decoding of movement parameters). There are also limitations in this work. For example, despite the comparatively large number of electrodes across the human brain in our study, the number of informative channels is still limited. In this point, the current analysis delivers an observation on most of the crucial regions involving the neural processing network under the current task, but may still not cover all of them. Besides, to make a robust group analysis, we combine the results of informative channels from both hemispheres during the computation of the average activation time of different ROIs, the generated result hence should be interpreted as a macro-level spatio-temporal evolution under the current task. Hence, recording from a larger number of channels will still be essential and valuable for further revealing the neural dynamics of the human brain in more detail. Notably, we have identified the neuronal representations as being ‘sensory’ or ‘motor’ for informative channels from multiple ROIs. Meanwhile, we also detected a number of channels occupying positions that are intermediate between these two extremes and can not be described by either label (Fig. 4d, DiCarlo and Maunsell (2005)). These channels generally display multiple firing patterns or present irregular neural responses that do not fit the two categories analyzed here. Making additional assessments of the functions for these channels presenting irregular firing patterns using new experiments or analysis methods (e.g., functional connectivity (Bastos and Schoffelen, 2015)) remains an important topic and deserves further investigation. Lastly, this study concentrates solely on the high-frequency component of the neural recordings, but some other simultaneous movement-relevant phenomena relating to the lower-frequency activity have been reported as well, such as the sensorimotor rhythm (SMR) in the mu and beta band and movement-related cortical potentials (MRCP) of the slow waves (Liu et al., 2020). What is largely unknown, is the relationship between these different measurements (e.g., the modulation of low-frequency activity to high-frequency ones) and the underlying mechanism between such relationship. In the future, it would be interesting to comprehensively address this question using a larger number of neural recordings.

## Funding

This work was supported by grants from the National Natural Science Foundation of China (Grant Nos. 52105030, 91948302, 91848112), Shanghai Municipal Science and Technology Major Project (Grant No. 2018SHZDZX01) and ZJLab, Medical and Engineering Cross Foundation of Shanghai Jiao Tong University (Grant No. AH0200003).

## Author Contributions

G. L., S. J., D. Z., L. C., and X. Z., designed research; G. L., S. J., Z. W., Z. F., and J. H., performed research; D. Z., L. C., and X. Z. supported with funding; G. L., S. J., J. M., and H. J. analyzed data; G. L., S. J., and G.S. wrote the paper; J. M., H. J., S. X., D. Z., L. C., and X. Z., reviewed and edited the paper.

## Data and Code Availability Statement

The human SEEG/ECog data required to reproduce these findings are available from the authors after reasonable request. The software used in this study can be downloaded through the link provided within the paper. Other associated protocols, codes,

and materials discussed in the paper will be made available to readers upon reasonable request.

## Notes

The authors of this article declare no competing interests.

## References

- Aflalo, T., Kellis, S., Klaes, C., Lee, B., Shi, Y., Pejsa, K., Shanfield, K., Hayes-Jackson, S., Aisen, M., Heck, C.. Decoding motor imagery from the posterior parietal cortex of a tetraplegic human. *Science* 2015;348(6237):906–910.
- Andersen, R.A., Buneo, C.A.. Intentional maps in posterior parietal cortex. *Annual Review of Neuroscience* 2002;25(1):189–220.
- Andersen, R.A., Cui, H.. Intention, action planning, and decision making in parietal-frontal circuits. *Neuron* 2009;63(5):568–83.
- Arnal, L.H., Kleinschmidt, A., Spinelli, L., Giraud, A.L., Megevand, P.. The rough sound of salience enhances aversion through neural synchronisation. *Nature Communications* 2019;10(1):3671.
- Avanzini, P., Abdollahi, R.O., Sartori, I., Caruana, F., Pelliccia, V., Casaceli, G., Mai, R., Lo Russo, G., Rizzolatti, G., Orban, G.A.. Four-dimensional maps of the human somatosensory system. *Proceedings of the National Academy of Sciences* 2016;113(13):E1936–43.
- Banerjee, A., Dean, H.L., Pesaran, B.. A likelihood method for computing selection times in spiking and local field potential activity. *Journal of Neurophysiology* 2010;104(6):3705–3720.
- Bartoli, E., Aron, A.R., Tandon, N.. Topography and timing of activity in right inferior frontal cortex and anterior insula for stopping movement. *Human Brain Mapping* 2018;39(1):189–203.
- Bartolomei, F., Nica, A., Valenti-Hirsch, M.P., Adam, C., Denuelle, M.. Interpretation of SEEG recordings. *Clinical Neurophysiology* 2018;48(1):53–57.
- Bassett, D.S., Wymbs, N.F., Porter, M.A., Mucha, P.J., Carlson, J.M., Grafton, S.T.. Dynamic reconfiguration of human brain networks during learning. *Proceedings of the National Academy of Sciences* 2011;108(18):7641–6.
- Bastos, A.M., Schoffelen, J.M.. A tutorial review of functional connectivity analysis methods and their interpretational pitfalls. *Frontiers in Systems Neuroscience* 2015;9:175.
- Betzel, R.F., Medaglia, J.D., Kahn, A.E., Soffer, J., Schonhaut, D.R., Bassett, D.S.. Structural, geometric and genetic factors predict interregional brain connectivity patterns probed by electrocorticography. *Nature Biomedical Engineering* 2019;3(11):902–916.
- Bonini, F., Burle, B., Ligeois-Chauvel, C., Rgis, J., Chauvel, P., Vidal, F.. Action monitoring and medial frontal cortex: Leading role of supplementary motor area. *Science* 2014;343(6173):888.
- Botvinick, M.M., Cohen, J.D.. The computational and neural basis of cognitive control: charted territory and new frontiers. *Cognitive Science* 2014;38(6):1249–85.
- Bressler, S.L., Menon, V.. Large-scale brain networks in cognition: emerging methods and principles. *Trends Cognitive Science* 2010;14(6):277–90.
- Brovelli, A., Badier, J.M., Bonini, F., Bartolomei, F., Coulon, O., Auzias, G.. Dynamic reconfiguration of visuomotor-related

- functional connectivity networks. *The Journal of Neuroscience* 2017;37(4):839–853.
- Brovelli, A., Chicharro, D., Badier, J.M., Wang, H., Jirsa, V.. Characterization of cortical networks and corticocortical functional connectivity mediating arbitrary visuomotor mapping. *The Journal of Neuroscience* 2015;35(37):12643–58.
- Buzsaki, G., Anastassiou, C.A., Koch, C.. The origin of extracellular fields and currents—EEG, ECoG, LFP and spikes. *Nature Reviews Neuroscience* 2012;13(6):407–20.
- Cardin, J.A., Carlén, M., Meletis, K., Knoblich, U., Zhang, F., Deisseroth, K., Tsai, L.H., Moore, C.I.. Driving fast-spiking cells induces gamma rhythm and controls sensory responses. *Nature* 2009;459:663.
- Caruana, F., Avanzini, P., Mai, R., Pelliccia, V., LoRusso, G., Rizzolatti, G., Orban, G.A.. Decomposing tool-action observation: A stereo-EEG study. *Cerebral Cortex* 2017;27(8):4229–4243.
- Cohen, D.. Magnetoencephalography: Evidence of magnetic fields produced by alpha-rhythm currents. *Science* 1968;161(3843):784–786.
- Cohen, M.X.. Where does EEG come from and what does it mean? *Trends in Neurosciences* 2017;40(4):208–218.
- Collins, D.L., Neelin, P., Peters, T.M., Evans, A.C.. Automatic 3D intersubject registration of MR volumetric data in standardized Talairach space. *Journal of computer assisted tomography* 1994;18(2):192–205.
- Conner, C.R., Chen, G., Pieters, T.A., Tandon, N.. Category specific spatial dissociations of parallel processes underlying visual naming. *Cerebral Cortex* 2014;24(10):2741–50.
- Coon, W.G., Gunduz, A., Brunner, P., Ritaccio, A.L., Pesaran, B., Schalk, G.. Oscillatory phase modulates the timing of neuronal activations and resulting behavior. *Neuroimage* 2016;133:294–301.
- Coon, W.G., Schalk, G.. A method to establish the spatiotemporal evolution of task-related cortical activity from electrocorticographic signals in single trials. *Journal of Neuroscience Methods* 2016;271:76–85.
- Corbetta, M., Shulman, G.L.. Control of goal-directed and stimulus-driven attention in the brain. *Nature Reviews Neuroscience* 2002;3(3):201–15.
- Culham, J.C., Valyear, K.F.. Human parietal cortex in action. *Current Opinion in Neurobiology* 2006;16(2):205–12.
- Del Percio, C., Derambure, P., Noce, G., Lizio, R., Bartres-Faz, D., Blin, O., Payoux, P., Deplanque, D., Meligne, D., Chauveau, N., Bourriez, J.L., Casse-Perrot, C., Lanteaume, L., Thalamas, C., Dukart, J., Ferri, R., Pascarelli, M.T., Richardson, J.C., Bordet, R., Babiloni, C., PharmaCog, C.. Sleep deprivation and modafinil affect cortical sources of resting state electroencephalographic rhythms in healthy young adults. *Clinical Neurophysiology* 2019;130(9):1488–1498.
- Desikan, R.S., Sgonne, F., Fischl, B., Quinn, B.T., Dickerson, B.C., Blacker, D., Buckner, R.L., Dale, A.M., Maguire, R.P., Hyman, B.T.. An automated labeling system for subdividing the human cerebral cortex on MRI scans into gyral based regions of interest. *Neuroimage* 2006;31(3):968–980.
- DiCarlo, J.J., Maunsell, J.H.. Using neuronal latency to determine sensory-motor processing pathways in reaction time tasks. *Journal of Neurophysiology* 2005;93(5):2974–86.
- Ding, Z., Huang, Y., Bailey, S.K., Gao, Y., Cutting, L.E., Rogers, B.P., Newton, A.T., Gore, J.C.. Detection of synchronous brain activity in white matter tracts at rest and under functional loading. *Proceedings of the National Academy of Sciences* 2018;115(3):595–600.
- Engel, A.K., Moll, C.K., Fried, I., Ojemann, G.A.. Invasive recordings from the human brain: clinical insights and beyond. *Nature Reviews Neuroscience* 2005;6(1):35–47.
- Fischl, B., Salat, D.H., Busa, E., Albert, M., Dieterich, M., Haselgrove, C., van der Kouwe, A., Killiany, R., Kennedy, D., Klaveness, S., Montillo, A., Makris, N., Rosen, B., Dale, A.M.. Whole brain segmentation. *Neuron* 2002;33(3):341–355.
- Floyer-Lea, A., Matthews, P.M.. Changing brain networks for visuomotor control with increased movement automaticity. *Journal of Neurophysiology* 2004;92(4):2405–2412.
- Franklin, D.W., Wolpert, D.M.. Computational mechanisms of sensorimotor control. *Neuron* 2011;72(3):425–42.
- Guevara, M., Roman, C., Houenou, J., Duclap, D., Poupon, C., Mangin, J.F., Guevara, P.. Reproducibility of superficial white matter tracts using diffusion-weighted imaging tractography. *Neuroimage* 2017;147:703–725.
- Haaland, K.Y., Elsinger, C.L., Mayer, A.R., Durgerian, S., Rao, S.M.. Motor sequence complexity and performing hand produce differential patterns of hemispheric lateralization. *Journal of Cognitive Neuroscience* 2004;16(4):621–636.
- Hauschild, M., Mulliken, G.H., Fineman, I., Loeb, G.E., Andersen, R.A.. Cognitive signals for brain-machine interfaces in posterior parietal cortex include continuous 3D trajectory commands. *Proceedings of the National Academy of Sciences* 2012;109(42):17075–80.
- Jerbi, K., Lachaux, J.P., N'Diaye, K., Pantazis, D., Leahy, R.M., Garnero, L., Baillet, S.. Coherent neural representation of hand speed in humans revealed by MEG imaging. *Proceedings of the National Academy of Sciences* 2007;104(18):7676–7681.
- Johnson, P.B., Ferraina, S., Bianchi, L., Caminiti, R.. Cortical networks for visual reaching: Physiological and anatomical organization of frontal and parietal lobe arm regions. *Cerebral Cortex* 1996;6(2):102–119.
- Keller, C.J., Honey, C.J., Entz, L., Bickel, S., Groppe, D.M., Toth, E., Ulbert, I., Lado, F.A., Mehta, A.D.. Corticocortical evoked potentials reveal projectors and integrators in human brain networks. *The Journal of Neuroscience* 2014;34(27):9152–63.
- Klaes, C., Kellis, S., Aflalo, T., Lee, B., Pejsa, K., Shanfield, K., Hayes-Jackson, S., Aisen, M., Heck, C., Liu, C., Andersen, R.A.. Hand shape representations in the human posterior parietal cortex. *The Journal of Neuroscience* 2015;35(46):15466–76.
- Kopell, N.J., Gritton, H.J., Whittington, M.A., Kramer, M.A.. Beyond the connectome: The dynamome. *Neuron* 2014;83(6):1319–1328.
- Koutsos, E., Paraskevopoulou, S.E., Constandinou, T.G.. A 1.5  $\mu\text{w}$  NEO-based spike detector with adaptive-threshold for calibration-free multichannel neural interfaces. In: 2013 IEEE International Symposium on Circuits and Systems (ISCAS2013). IEEE; 2013. p. 1922–1925.
- Króliczak, G., Frey, S.H.. A common network in the left cerebral hemisphere represents planning of tool use pantomimes and familiar intransitive gestures at the hand-independent level. *Cerebral Cortex* 2009;19(10):2396–410.
- Kuang, S., Morel, P., Gail, A.. Planning movements in visual and physical space in monkey posterior parietal cortex. *Cerebral Cortex* 2016;26(2):731–47.

- Lachaux, J.P., Axmacher, N., Mormann, F., Halgren, E., Crone, N.E.. High-frequency neural activity and human cognition: past, present and possible future of intracranial EEG research. *Progress in Neurobiology* 2012;98(3):279–301.
- Lachaux, J.P., Rudrauf, D., Kahane, P.. Intracranial EEG and human brain mapping. *Journal of Physiology-Paris* 2003;97(4):613–628.
- Larsson, J., Heeger, D.J.. Two retinotopic visual areas in human lateral occipital cortex. *The Journal of Neuroscience* 2006;26(51):13128–13142.
- Lebedev, M.A., Nicolelis, M.A.. Brain-machine interfaces: From basic science to neuroprostheses and neurorehabilitation. *Physiological Reviews* 2017;97(2):767–837.
- Ledberg, A., Bressler, S.L., Ding, M., Coppola, R., Nakamura, R.. Large-scale visuomotor integration in the cerebral cortex. *Cerebral Cortex* 2007;17(1):44–62.
- Lemon, R.N.. Descending pathways in motor control. *Annual Review of Neuroscience* 2008;31:195–218.
- Li, G., Jiang, S., Chen, C., Brunner, P., Wu, Z., Schalk, G., Chen, L., Zhang, D.. iEEGview: an open-source multifunction GUI-based Matlab toolbox for localization and visualization of human intracranial electrodes. *Journal of Neural Engineering* 2019;17(1):016016.
- Li, G., Jiang, S., Meng, J., Chai, G., Wu, Z., Fan, Z., Hu, J., Sheng, X., Zhang, D., Chen, L., Zhu, X.. Assessing differential representation of hand movements in multiple domains using stereo-electroencephalographic recordings. *Neuroimage* 2022;250:118969.
- Li, G., Jiang, S., Paraskevopoulou, S.E., Chai, G., Wei, Z., Liu, S., Wang, M., Xu, Y., Fan, Z., Wu, Z., Chen, L., Zhang, D., Zhu, X.. Detection of human white matter activation and evaluation of its function in movement decoding using stereo-electroencephalography (SEEG). *Journal of Neural Engineering* 2021;18(4):0460c6.
- Li, G., Jiang, S., Paraskevopoulou, S.E., Wang, M., Xu, Y., Wu, Z., Chen, L., Zhang, D., Schalk, G.. Optimal referencing for stereo-electroencephalographic (SEEG) recordings. *Neuroimage* 2018;183:327–335.
- Liu, S., Li, G., Jiang, S., Wu, X., Hu, J., Zhang, D., Chen, L.. Investigating data cleaning methods to improve performance of brain-computer interfaces based on stereo-electroencephalography. *Frontiers in neuroscience* 2021;15:725384–725384.
- Liu, T., Huang, G., Jiang, N., Yao, L., Zhang, Z.. Reduce brain computer interface inefficiency by combining sensory motor rhythm and movement-related cortical potential features. *Journal of Neural Engineering* 2020;17(3):035003.
- Manning, J.R., Jacobs, J., Fried, I., Kahana, M.J.. Broadband shifts in local field potential power spectra are correlated with single-neuron spiking in humans. *The Journal of Neuroscience* 2009;29(43):13613–20.
- Maragos, P., Kaiser, J.F., Quatieri, T.F.. On amplitude and frequency demodulation using energy operators. *IEEE Transactions on Signal Processing* 1993;41(4):1532–1550.
- Miller, E.K., Cohen, J.D.. An integrative theory of prefrontal cortex function. *Annual Review of Neuroscience* 2001;24(1):167–202.
- Miller, K.J., Honey, C.J., Hermes, D., Rao, R.P., denNijs, M., Ojemann, J.G.. Broadband changes in the cortical surface potential track activation of functionally diverse neuronal populations. *Neuroimage* 2014;85:711–720.
- Miller, K.J., Schalk, G., Fetz, E.E., den Nijs, M., Ojemann, J.G., Rao, R.P.N.. Cortical activity during motor execution, motor imagery, and imagery-based online feedback. *Proceedings of the National Academy of Sciences* 2010;107(9):4430.
- Molholm, S., Sehatpour, P., Mehta, A.D., Shpaner, M., Gomez-Ramirez, M., Ortigue, S., Dyke, J.P., Schwartz, T.H., Foxe, J.J.. Audio-visual multisensory integration in superior parietal lobule revealed by human intracranial recordings. *Journal of Neurophysiology* 2006;96(2):721–9.
- Nir, Y., Fisch, L., Mukamel, R., Gelbard-Sagiv, H., Arieli, A., Fried, I., Malach, R.. Coupling between neuronal firing rate, gamma LFP, and BOLD fMRI is related to interneuronal correlations. *Current Biology* 2007;17(15):1275–85.
- Nishitani, N., Hari, R.. Temporal dynamics of cortical representation for action. *Proceedings of the National Academy of Sciences* 2000;97(2):913.
- Oishi, K., Zilles, K., Amunts, K., Faria, A., Jiang, H., Li, X., Akhter, K., Hua, K., Woods, R., Toga, A.W., Pike, G.B., Rosa-Neto, P., Evans, A., Zhang, J., Huang, H., Miller, M.I., van Zijl, P.C., Mazziotta, J., Mori, S.. Human brain white matter atlas: identification and assignment of common anatomical structures in superficial white matter. *Neuroimage* 2008;43(3):447–57.
- Oosterhof, N.N., Tipper, S.P., Downing, P.E.. Visuo-motor imagery of specific manual actions: a multi-variate pattern analysis fMRI study. *Neuroimage* 2012;63(1):262–71.
- Paraskevopoulou, S.E., Coon, W.G., Brunner, P., Miller, K.J., Schalk, G.. Within-subject reaction time variability: Role of cortical networks and underlying neurophysiological mechanisms. *Neuroimage* 2021;237:118127.
- Parvizi, J., Kastner, S.. Promises and limitations of human intracranial electroencephalography. *Nature Neuroscience* 2018;21(4):474–483.
- de Pasquale, F., Della Penna, S., Snyder, A.Z., Lewis, C., Mantini, D., Marzetti, L., Belardinelli, P., Ciancetta, L., Pizzella, V., Romani, G.L., Corbetta, M.. Temporal dynamics of spontaneous MEG activity in brain networks. *Proceedings of the National Academy of Sciences* 2010;107(13):6040–5.
- Pei, X., Leuthardt, E.C., Gaona, C.M., Brunner, P., Wolpaw, J.R., Schalk, G.. Spatiotemporal dynamics of electrocorticographic high gamma activity during overt and covert word repetition. *Neuroimage* 2011;54(4):2960–72.
- Perel, S., Sadtler, P.T., Oby, E.R., Ryu, S.I., Tyler-Kabara, E.C., Batista, A.P., Chase, S.M.. Single-unit activity, threshold crossings, and local field potentials in motor cortex differentially encode reach kinematics. *Journal of Neurophysiology* 2015;114(3):1500–12.
- Pesaran, B., Vinck, M., Einevoll, G.T., Sirota, A., Fries, P., Siegel, M., Truccolo, W., Schroeder, C.E., Srinivasan, R.. Investigating large-scale brain dynamics using field potential recordings: analysis and interpretation. *Nature Neuroscience* 2018;21(7):903–919.
- Posner, M., Szczepanski, S.M., Crone, N.E., Kuperman, R.A., Augustine, K.I., Parvizi, J., Knight, R.T.. Dynamic changes in phase-amplitude coupling facilitate spatial attention control in fronto-parietal cortex. *PLoS Biology* 2014;12(8):e1001936.
- Rao, N.G., Donoghue, J.P.. Cue to action processing in motor cortex populations. *Journal of Neurophysiology* 2014;111(2):441–53.
- Ray, S., Crone, N.E., Niebur, E., Franaszczuk, P.J., Hsiao, S.S.. Neural correlates of high-gamma oscillations

- (60-200 Hz) in macaque local field potentials and their potential implications in electrocorticography. *The Journal of Neuroscience* 2008;28(45):11526–36.
- Reichenbach, A., Franklin, D.W., Zatska-Haas, P., Diedrichsen, J.. A dedicated binding mechanism for the visual control of movement. *Current Biology* 2014;24(7):780–5.
- Rey, H.G., Ahmadi, M., Quiñero, R.. Single trial analysis of field potentials in perception, learning and memory. *Current Opinion in Neurobiology* 2015;31:148–55.
- Ries, S.K., Dhillon, R.K., Clarke, A., King-Stephens, D., Laxer, K.D., Weber, P.B., Kuperman, R.A., Auguste, K.I., Brunner, P., Schalk, G., Lin, J.J., Parvizi, J., Crone, N.E., Dronkers, N.F., Knight, R.T.. Spatiotemporal dynamics of word retrieval in speech production revealed by cortical high-frequency band activity. *Proceedings of the National Academy of Sciences* 2017;114(23):E4530–E4538.
- Rizzolatti, G., Cattaneo, L., Fabbri-Destro, M., Rozzi, S.. Cortical mechanisms underlying the organization of goal-directed actions and mirror neuron-based action understanding. *Physiological Reviews* 2014;94(2):655–706.
- Sakkalis, V.. Review of advanced techniques for the estimation of brain connectivity measured with EEG/MEG. *Computers in Biology and Medicine* 2011;41(12):1110–7.
- Salat, D.H., Lee, S.Y., van der Kouwe, A.J., Greve, D.N., Fischl, B., Rosas, H.D.. Age-associated alterations in cortical gray and white matter signal intensity and gray to white matter contrast. *Neuroimage* 2009;48(1):21–8.
- Schalk, G., Kapeller, C., Guger, C., Ogawa, H., Hiroshima, S., Lafer-Sousa, R., Saygin, Z.M., Kamada, K., Kanwisher, N.. Facephenes and rainbows: Causal evidence for functional and anatomical specificity of face and color processing in the human brain. *Proceedings of the National Academy of Sciences* 2017a;114(46):12285–12290.
- Schalk, G., Kubanek, J., Miller, K.J., Anderson, N.R., Leuthardt, E.C., Ojemann, J.G., Limbrick, D., Moran, D., Gerhardt, L.A., Wolpaw, J.R.. Decoding two-dimensional movement trajectories using electrocorticographic signals in humans. *Journal of Neural Engineering* 2007;4(3):264–75.
- Schalk, G., Marple, J., Knight, R.T., Coon, W.G.. Instantaneous voltage as an alternative to power- and phase-based interpretation of oscillatory brain activity. *Neuroimage* 2017b;157:545–554.
- Schall, J.D.. Visuomotor functions in the frontal lobe. *Annual Review of Vision Science* 2015;1:469–498.
- Scott, S.H.. Optimal feedback control and the neural basis of volitional motor control. *Nature Reviews Neuroscience* 2004;5(7):532–46.
- Sedghamiz, H.. BioSigKit: A Matlab toolbox and interface for analysis of biosignals. *Journal of Open Source Software* 2018;3(30):671.
- Sun, H., Blakely, T.M., Darvas, F., Wander, J.D., Johnson, L.A., Su, D.K., Miller, K.J., Fetz, E.E., Ojemann, J.G.. Sequential activation of premotor, primary somatosensory and primary motor areas in humans during cued finger movements. *Clinical Neurophysiology* 2015;126(11):2150–61.
- Takahashi, K., Kim, S., Coleman, T.P., Brown, K.A., Suminski, A.J., Best, M.D., Hatsopoulos, N.G.. Large-scale spatiotemporal spike patterning consistent with wave propagation in motor cortex. *Nature Communications* 2015;6:7169.
- Tallon-Baudry, C., Bertrand, O., Hénaff, M.A., Isnard, J., Fischer, C.. Attention modulates gamma-band oscillations differently in the human lateral occipital cortex and fusiform gyrus. *Cerebral Cortex* 2004;15(5):654–662.
- Thiery, T., Saive, A.L., Combrissin, E., Dehgan, A., Bastin, J., Kahane, P., Berthoz, A., Lachaux, J.P., Jerbi, K.. Decoding the neural dynamics of free choice in humans. *PLoS Biology* 2020;18(12):e3000864–e3000864.
- Thurer, B., Stockinger, C., Focke, A., Putze, F., Schultz, T., Stein, T.. Increased gamma band power during movement planning coincides with motor memory retrieval. *Neuroimage* 2016;125:172–181.
- Vingerhoets, G., Acke, F., Alderweireldt, A.S., Nys, J., Vandemaele, P., Achten, E.. Cerebral lateralization of praxis in right- and left-handedness: same pattern, different strength. *Human Brain Mapping* 2012;33(4):763–77.
- Voytek, B., Kayser, A.S., Badre, D., Fegen, D., Chang, E.F., Crone, N.E., Parvizi, J., Knight, R.T., D’Esposito, M.. Oscillatory dynamics coordinating human frontal networks in support of goal maintenance. *Nature Neuroscience* 2015;18(9):1318–1324.
- Wander, J.D., Blakely, T., Miller, K.J., Weaver, K.E., Johnson, L.A., Olson, J.D., Fetz, E.E., Rao, R.P.N., Ojemann, J.G.. Distributed cortical adaptation during learning of a brain-computer interface task. *Proceedings of the National Academy of Sciences* 2013;110(26):10818–10823.
- Wang, M., Li, G., Jiang, S., Wei, Z., Hu, J., Chen, L., Zhang, D.. Enhancing gesture decoding performance using signals from posterior parietal cortex: a stereo-electroencephalography (SEEG) study. *Journal of Neural Engineering* 2020;17(4):046043.
- Wolpert, D., Ghahramani, Z., Jordan, M.. An internal model for sensorimotor integration. *Science* 1995;269(5232):1880–1882.
- Zalesky, A., Fornito, A., Cocchi, L., Gollo, L.L., Breakspear, M.. Time-resolved resting-state brain networks. *Proceedings of the National Academy of Sciences* 2014;111(28):10341–6.



---

# Supplementary Materials for Spatio-temporal Evolution of Human Neural Activity During Visually-cued Hand Movements

**This PDF file includes:**

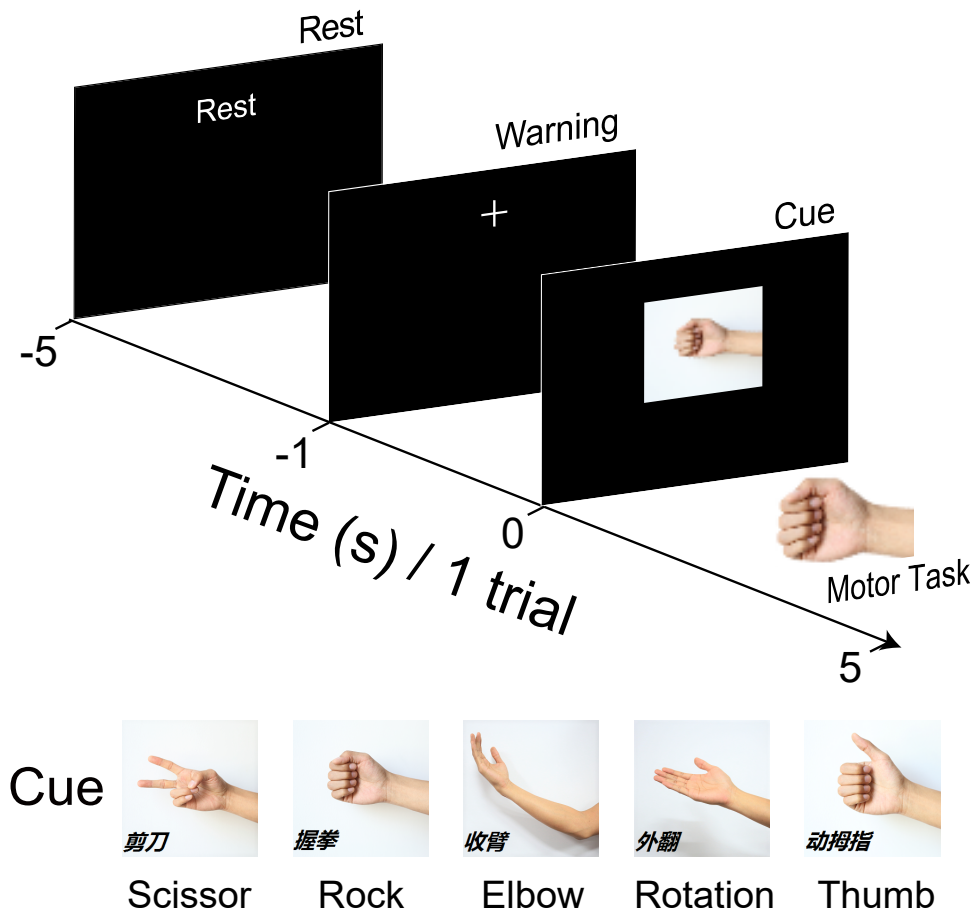
Table S1 and S2  
Figures S1 to S6

**Supplementary Table 1.** Clinical profiles of all 36 subjects that participated in the study. Among these subjects, 34 were implanted with SEEG depth electrodes, and 2 (Sub. 32, Sub. 35) were implanted with ECoG grid electrodes. Abbreviations for this table: RS (Recording hemisphere), SR (Sampling rate), EL (Number of electrode shafts), CH (Number of contacts), OH (Operating hand during the experiment), TH (Cut-off threshold during the line noise detection for each subject, see Sec. Data Pre-Processing of Materials and Methods), BC (Bad Channel, i.e., Number of channels whose line noise power exceeds the cut-off threshold).

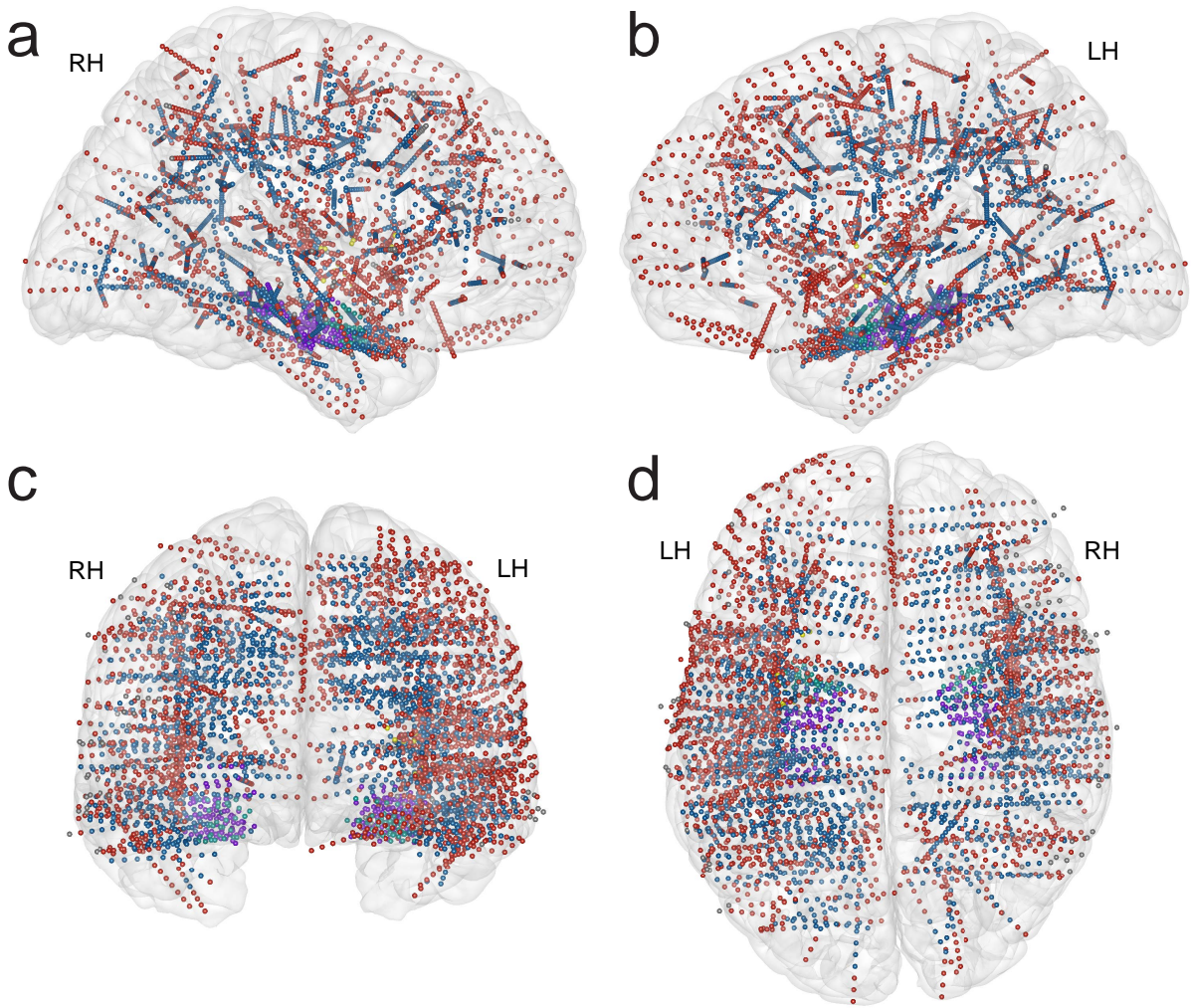
Sub ID	Gender	Age	RS	SR (Hz)	EL	CH	OH	TH ( $\mu$ V)	BC
1	M	23	Left	1000	10	121	Right	32.76	2
2	M	33	Left	1000	15	180	Right	68.43	1
3	F	30	Right	1000	7	60	Left	24.17	0
4	M	26	Right	1000	13	178	Left	30.16	1
5	M	25	Right	1000	10	143	Left	41.63	0
6	F	17	Bilateral	1000	13	169	Left	3.24	2
7	F	28	Right	1000	9	114	Left	77.02	0
8	M	27	Left	2000	16	208	Right	36.67	0
9	M	15	Bilateral	500	13	194	Left	7.97	3
10	M	31	Right	500	6	94	Left	3.34	2
11	F	22	Left	2000	7	102	Right	2.66	0
12	M	19	Bilateral	2000	9	130	Left	5.68	0
13	F	30	Bilateral	2000	13	170	Right	4.56	0
14	M	31	Left	2000	10	144	Right	2.99	5
15	M	27	Bilateral	2000	10	144	Right	7.18	1
16	M	16	Bilateral	2000	13	137	Right	6.73	8
17	M	24	Right	1000	8	108	Left	10.27	1
18	F	30	Left	1000	9	118	Right	2.90	4
19	F	33	Left	2000	12	150	Right	10.94	2
20	F	23	Bilateral	2000	15	198	Right	6.40	3
21	F	23	Right	2000	10	130	Left	2.83	2
22	F	42	Left	2000	10	137	Right	8.29	1
23	M	33	Bilateral	2000	11	154	Right	14.34	1
24	M	15	Left	2000	8	110	Right	7.27	0
25	M	25	Bilateral	2000	8	108	Left	12.72	2
26	M	29	Bilateral	2000	5	72	Right	2.30	2
27	M	22	Bilateral	2000	6	56	Left	3.83	0
28	M	15	Right	2000	7	102	Left	34.06	1
29	M	26	Left	1000	10	136	Right	58.83	0
30	F	27	Bilateral	2000	10	117	Right	16.82	3
31	F	27	Bilateral	2000	6	64	Right	104.52	0
32	F	19	Left	2000	N/A	242	Right	1555.17	1
33	M	32	Bilateral	2000	9	126	Left	19.57	0
34	F	35	Right	2000	15	190	Left	29.25	0
35	M	26	Left	2000	N/A	208	Right	28.90	0
36	M	31	Left	2000	11	172	Right	34.65	0

**Supplementary Table 2.** Information of brain regions reported in this study. Electrode number indicates the number of electrodes implanted in the listed brain region across all 36 subjects.

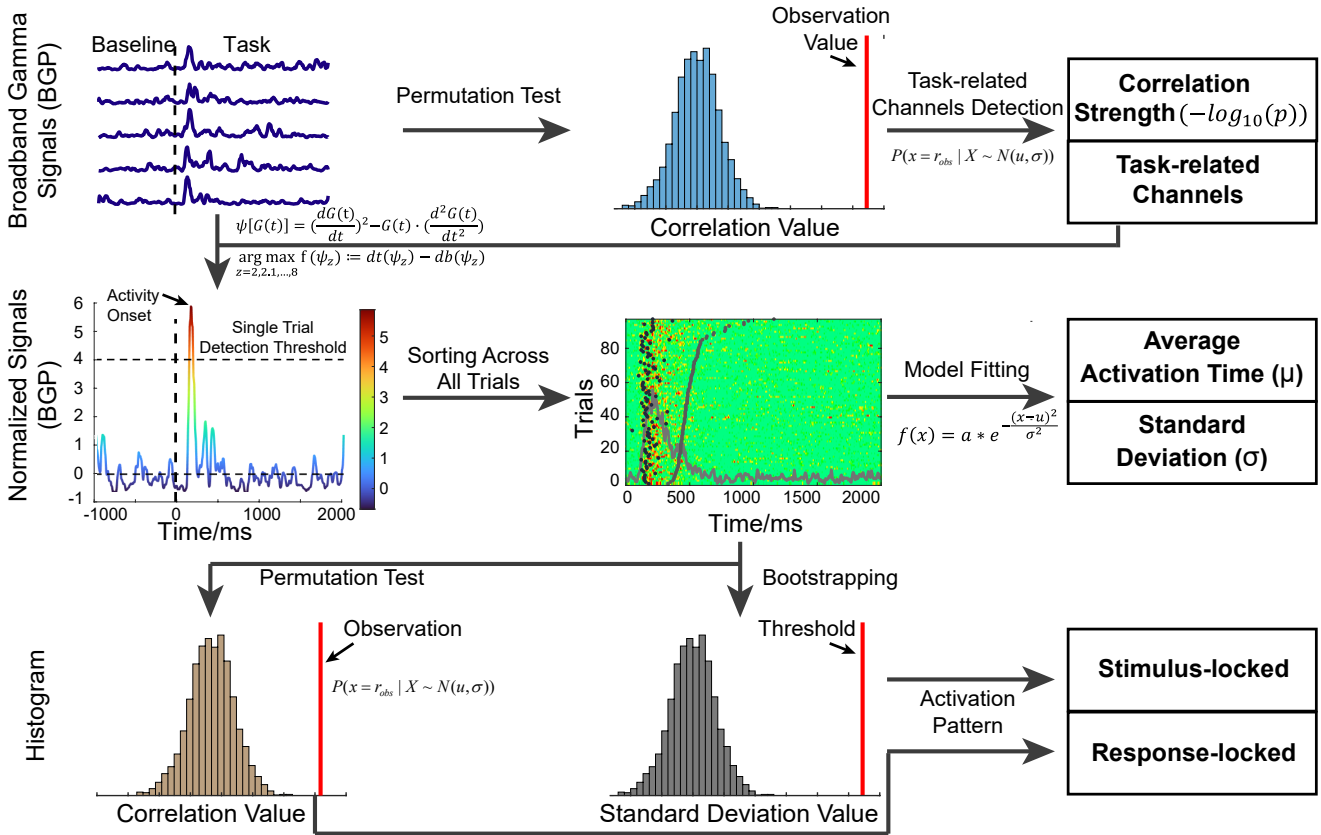
ID	Brain Regions	Abbreviation	Electrode Number	Groups
1	superior frontal gyrus	SFG	245	Frontal Area
2	rostral middle frontal gyrus	rMFG	311	
3	caudal middle frontal gyrus	cMFG	174	
4	lateral orbitofrontal gyrus	OFG	54	
5	pars opercularis	parsOPE	119	
6	parstriangularis	parsTRI	98	
7	parsorbitalis	parsORB	32	
8	precentral cortex	PRC	368	Central Area
9	postcentral cortex	POC	213	
10	paracentral cortex	PAC	56	
1	superior parietal cortex	SPC	182	Parietal Area
12	inferior parietal cortex	IPC	206	
13	supramarginal gyrus	SMG	261	
14	precuneus cortex	PNC	183	
15	superior temporal gyrus	STG	390	Temporal Area
16	inferior temporal gyrus	ITG	193	
17	middle temporal gyrus	MTG	325	
18	transverse temporal gyrus	TTG	43	
19	fusiform gyrus	FFG	102	
20	banks of the superior temporal sulcus	bankssts	53	
21	lateral occipital cortex	LOC	74	Occipital Area
22	pericalcarine cortex	PCC	33	
23	lingual gyrus	LGG	62	
24	cuneus cortex	CNC	18	
25	insula cortex	ISC	374	Insula
26	parahippocampal gyrus	PHG	50	Limbic System
27	posterior cingulate gyrus	PCG	77	
28	Hippocampus	N/A	196	
29	caudal anterior cingulate gyrus	cACG	49	
30	rostral anterior cingulate gyrus	rACG	25	
31	Amygdala	N/A	85	



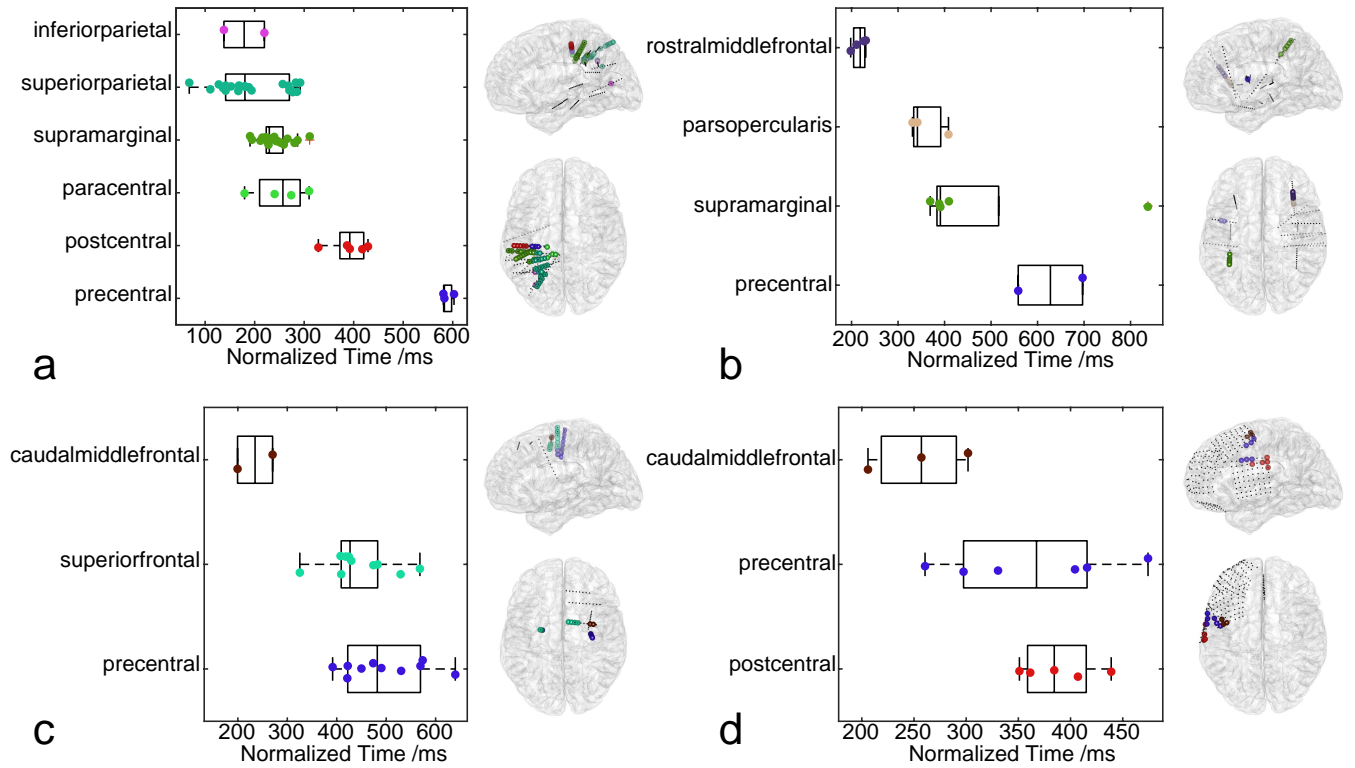
**Supplementary Figure 1.** Experiment protocol of the current study. Each subject performed five different hand or arm movements (see Cue). In each trial, one of five tasks was randomly selected and displayed (Cue, the onset of movement cue was set as time 0 in this study). They performed each type of movement 20 times (5 s each, [0, 5] s). Before the movement, each subject rested for 4 s ([-5, -1] s), and then a warning sign ([-1, 0] s) prompted the subject for movement initiation.



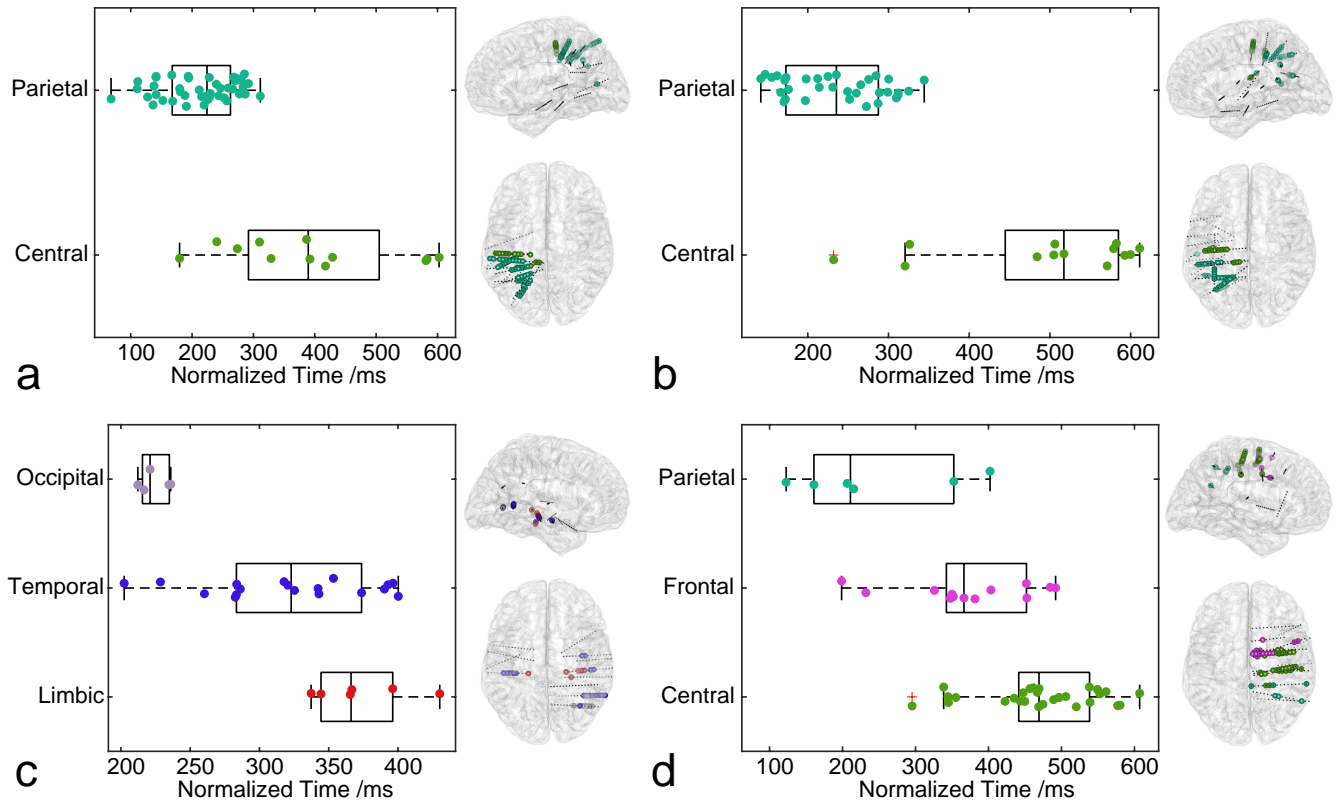
**Supplementary Figure 2.** Electrodes localization results of all 36 subjects. a)/b)/c)/d) Right/Left/Frontal/Top view of all the electrodes projected to the standard Montreal Neurological Institute (MNI) template. The electrodes (SEEG and ECoG) are shown with small balls. Different colors indicate different anatomical positions, where the red indicates the gray matter, the blue indicates the white matter, the purple indicates the hippocampus, the dark green indicates the amygdala, the yellow indicates the putamen and the gray indicates the other structures. LH/RH: Left/Right hemisphere.



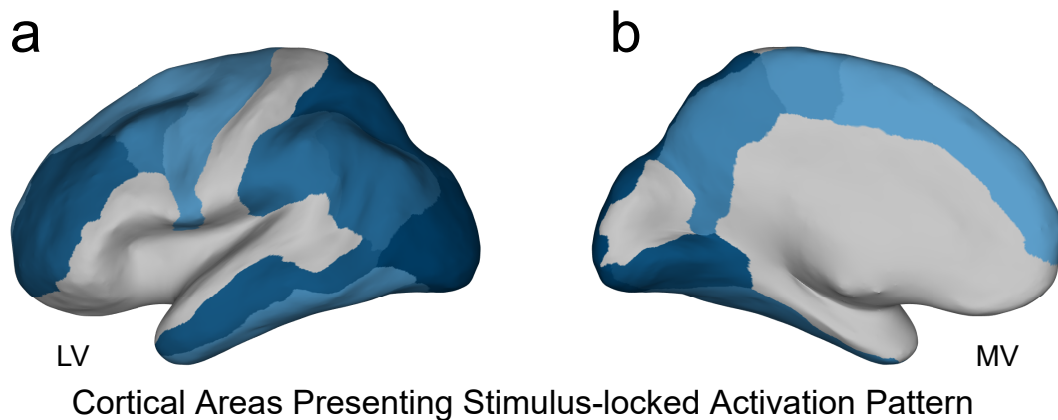
**Supplementary Figure 3.** The illustration of data processing in this work. The flow chart corresponds to the data processing from the section (Methods: Data Pre-Processing) to the section (Methods: Activation Pattern Evaluation). Specifically, to identify the response-locked channels (left lower subfigure), we first computed Pearson's correlation for the detected neural activation of each informative channel and the EMG onsets across all trials. Then, the sequence of detected neural activation was randomly shuffled and the correlation with the EMG onsets was computed again. This procedure was repeated 2500 times, thus, generating a distribution of surrogate correlation value (the histogram) and the subsequent  $p$  value (vertical red line) for the observed correlation value. The channel whose  $p$  value was smaller than the significance level ( $p < 0.05$  after Bonferroni correction) was identified as the response-locked channel. To identify the stimulus-locked channels (right lower subfigure), for each informative channel, the standard deviation of detected neural activation from randomly selected 60 trials was first computed. Then, this process was repeated for  $10^6$  times and the average standard deviation of these repetitions (the histogram) was obtained for each channel. The channel whose average standard deviation is smaller than the threshold (vertical red line) is identified as the stimulus-locked channel (see Methods: Activation Pattern Evaluation for more details).



**Supplementary Figure 4.** The spatio-temporal activation results during the task from four typical subjects (Sub. 02 (a), Sub. 06 (b), Sub. 27 (c), Sub. 32 (d)). The results are presented in groups based on the region of interest (ROI) where each informative electrode of this subject is located (same as Fig. 3a/e/f, see also Supplementary Table 2). **a)** The neural activation time of different ROIs from a single subject (Sub. 02). The boxplot presents the distribution of neural activation time for all the samples detected within each ROI. The colored dot indicates the result of each informative electrode. The vertical line within the boxplot indicates the median value. The right subfigure presents the position of each informative electrode (colored the same as the left subfigure) in the MNI brain. The black dots denote all the electrodes implanted for this subject. **b)/c)/d)** Results from the other typical subjects. Same configurations as a).



**Supplementary Figure 5.** The spatio-temporal activation results during the task from four typical subjects (Sub. 02 (a), Sub. 08 (b), Sub. 09 (c), Sub. 34 (d)). The results are presented in groups based on the broader brain area where each informative electrode of this subject is located (same as Fig. 3d/g/h, see also Supplementary Table 2). **a)** The neural activation time of different broader brain areas from a single subject (Sub. 02). The boxplot in the left subfigure presents the distribution of neural activation time for all the samples detected within each broader brain area. The colored dot indicates the result of each informative electrode. The vertical line within the boxplot indicates the median value. The right subfigure presents the position of each informative electrode (colored the same as the left subfigure) in the MNI brain. The black dots denote all the electrodes implanted for this subject. **b)/c)/d)** Results from the other typical subjects. Same configurations as a).



**Supplementary Figure 6.** Left(a)/Middle(b) view of the distribution of stimulus-locked channels on a flattened MNI brain. Results are shown with the left hemisphere only. The darkness of the colored cortex indicates the percentage value shown in Fig.4d of the main content. Darker color indicates a higher percentage. See Methods: Activation Pattern Evaluation for more details.